



24 April 2024

This is the final peer-reviewed accepted manuscript of:

Mastromarco, M., Manna, A., Aberle, O. et al. Cross section measurements of $^{155,157}\text{Gd}(n,\gamma)$ induced by thermal and epithermal neutrons. Eur. Phys. J. A 55, 9 (2019).

The final published version is available online at:
<https://doi.org/10.1140/epja/i2019-12692-7>

Rights / License:

The terms and conditions for the reuse of this version of the manuscript are specified in the publishing policy. For all terms of use and more information see the publisher's website.

This item was downloaded from IRIS Università di Bologna (<https://cris.unibo.it/>)

When citing, please refer to the published version.

Cross section measurements of $^{155,157}\text{Gd}(n,\gamma)$ induced by thermal and epithermal neutrons

M. Mastromarco¹, A. Manna^{2,3}, and
the n-TOF Collaboration

¹ Istituto Nazionale di Fisica Nucleare, Sezione di Bari, Italy

² Istituto Nazionale di Fisica Nucleare, Sezione di Bologna, Italy

³ Dipartimento di Fisica e Astronomia, Università di Bologna, Italy

⁴

Received: date / Revised version: date

Abstract. Neutron capture cross section measurements on ^{155}Gd and ^{157}Gd were performed using the time-of-flight technique at the n-TOF facility at CERN on isotopically enriched samples. The measurements were carried out in the n-TOF experimental area EAR1, at 185 m from the neutron source, with an array of 4 C_6D_6 liquid scintillation detectors. At a neutron kinetic energy of 0.0253 eV, capture cross sections of 62.2(2.2) and 239.8(8.4) kilobarn have been derived for ^{155}Gd and ^{157}Gd , respectively, with up to 6% deviation relative to values presently reported in nuclear data libraries, but consistent with those values within 1.6 standard deviations. A resonance shape analysis has been performed in the resolved resonance region up to 181 eV and 307 eV, respectively for ^{155}Gd and ^{157}Gd , where on average, resonance parameters have been found in good agreement with evaluations. Above these energies and up to 1 keV, the observed resonance-like structure of the cross section has been analysed and characterised. From a statistical analysis of the observed neutron resonances we deduced: neutron strength function of $2.01(28) \times 10^{-4}$ and $2.17(41) \times 10^{-4}$; average total radiative width of 106.8(14) meV and 101.1(20) meV and s -wave resonance spacing 1.6(2) eV and 4.8(5) eV for $n+^{155}\text{Gd}$ and $n+^{157}\text{Gd}$ systems, respectively.

PACS. XX.XX.XX No PACS code given

1 Introduction

The natural element with the highest cross section for thermal neutrons is gadolinium. Among its 7 stable isotopes, ^{157}Gd and, to a smaller extent, ^{155}Gd are responsible for this feature, mainly due to the presence of a neutron resonance near thermal energy (i. e. neutron kinetic energy $E_n = 0.0253$ eV, corresponding to a velocity of 2200 m/s). Given this peculiarity, accurate values of the neutron capture cross section of gadolinium isotopes are required in a variety of fields: for the understanding of the nucleosynthesis of heavy elements (beyond iron) in stars via the s and r processes [1]; for cancer neutron capture therapy [2]; for the development of neutrino detectors [3] and for nuclear technologies. In the last case, neutron cross section data have a relevant role in the neutron balance and in the safety features of Light Water Reactors and in Canada deuterium uranium (CANDU) reactor types, where gadolinium is used as burnable poison in the fuel pins or in the moderator of the reactor core [4].

A summary of the values of the thermal cross sections retrieved from the experimental nuclear reaction database EXFOR is reported in historical progression in Tab. 1 together with ENDF/B-VIII.0 [5], JEFF-3.3 [6], and JENDL-

4.0 [7] nuclear data libraries and the compilation by Mughabghab [8]. The measurements of Pattenden [12], Tattersall [13] and Choi [14] (reporting cross sections of 56.7(2.1) and 239(6) kbarn for ^{155}Gd and ^{157}Gd , respectively) are not listed because they are not direct measurements and depend on model calculations. Other measurements are reported by Noguere and collaborators [15] and Kang and collaborators [16]. The latter is a capture measurement and confirms the results by Leinweber et. al., whereas the work by Noguere et. al. reports a thermal neutron capture on ^{155}Gd of 61.9(1.5) kb. In general, the evaluated data files agree on the adoption of the $^{157}\text{Gd}(n,\gamma)$ thermal cross section consistent with the experiment by Ref. [9], although that value is about 12% higher than what was measured by Leinweber and collaborators [11] in a capture and transmission experiment. At higher energies, up to about 300 eV and especially beyond 181 eV (where the evaluations of ^{155}Gd terminate) isotopic resonance assignment in the literature are not consistent and thus evaluations reflect these doubtful assignments. Moreover, the resonance parameters deduced from the measurement of Leinweber and collaborators [11] are significantly different from the ENDF/B-VIII.0 and JEFF-3.3 evaluations.

Table 1. ^{155}Gd and ^{157}Gd thermal cross sections (in kb) as reported in literature, compilation [8] and evaluations.

Reference	Year	Thermal cross section	
		$n + ^{155}\text{Gd}$	$n + ^{157}\text{Gd}$
Møller [9]	1960	58.9(5) ^a	254(2) ^a
Ohno [10]	1968	61.9(6) ^a	248(4) ^a
Leinweber [11]	2006	60.2 ^b	226 ^b
Mughabghab	2009	60.9(0.5)	254.0(0.8)
JENDL-4.0	2016	60.735	253.25
JEFF-3.3	2017	60.89	254.5
ENDF/B-VIII.0	2018	60.89	253.32

^a Total cross section.^b The uncertainty is not explicitly quoted in Ref. [11].

However, this large deviation is not completely confirmed by a capture measurement on ^{155}Gd [17].

All these inconsistencies prompted an initiative to perform a new measurement of the capture cross section for the odd-mass gadolinium isotopes in the resolved resonance region, at the CERN neutron time-of-flight facility n_TOF [18]. In this work, we report the results of these measurements on ^{155}Gd and ^{157}Gd . In Sec. 2 the experimental conditions are discussed, while Sec. 3 describes the data reduction procedure together with the estimation of uncertainties on the results. Section 4 summarises the neutron resonance analysis: results and discussions for $^{155}\text{Gd}(n,\gamma)$ and $^{157}\text{Gd}(n,\gamma)$ are reported in Sec. 4.1 and 4.2, respectively. A resonance analysis above the resolved resonance region is reported in Appendix A.1.

2 Capture experiment

The $^{155}\text{Gd}(n,\gamma)$ and $^{157}\text{Gd}(n,\gamma)$ cross section measurements were performed in 2016 at the n_TOF 185-m station, using an array of 4 C_6D_6 detectors. The enriched gadolinium samples were in the form of self-supporting metal discs. Since the capture cross section for both isotopes drops by several orders of magnitude for neutron energies higher than 1 eV, two samples of different thickness for each isotope were used to obtain accurate results from the measurement in the whole energy range of interest, i. e. up to 1 keV.

2.1 The n_TOF spectrometer

The n_TOF facility features two white-spectra neutron beam lines, generated by 20 GeV/c protons impinging on a massive lead target, 40 cm in length and 60 cm in diameter. The present measurement was performed at the experimental area EAR1, at the nominal distance of 185 m from the spallation target, optimising the best resolving power of the spectrometer. At n_TOF, incident pulses of 7×10^{12} protons produce a total of 2×10^{15} neutrons/pulse. The neutron beam is collimated towards EAR1 by several elements [18], the last one of which is a 0.9-cm-radius collimator, set at 178 m from the target. Consequently, the

reduction of the neutron intensity attributable to the solid angle subtended by the collimator is of the order of 10^{-9} . The initially fast neutron spectrum of the target station is moderated by a first layer of 1 cm of demineralised water, complemented by a second layer of 4 cm of borated water ($\text{H}_2\text{O} + 1.28\%\text{H}_3\text{BO}_3$, fraction in mass). With this assembly, the energy spectrum of neutrons entering the flight path ranges from thermal energies up to the GeV region. Neutron pulses are produced with a frequency of about 1 Hz, thus completely preventing the overlap of slow neutrons between bunches.

The relative energy resolution, $\Delta E_n/E_n$, where ΔE can be considered the full width at half maximum of the energy distribution of the neutron beam at a given time-of-flight (or energy), is of the order of 3.2×10^{-4} at 1 eV and 5.4×10^{-4} at 1 keV (more details in Ref. [18] and [19]). Therefore, the resolution of the n_TOF spectrometer is smaller than the total width of neutron resonances in Gd up to about $E_n = 250$ eV. On the other hand, the Doppler broadening at EAR1 temperature (related to the thermal motion of the atoms in the sample) has a FWHM of $\approx 6, 150, 300$ and 600 meV at $E_n = 0.02, 12.5, 50$ and 200 eV, respectively. Therefore, the Doppler component starts to dominate the width of the observed resonance profile above 10 eV.

2.2 Capture detectors and instrumentation

The measurements were performed using an array of four deuterated benzene (C_6D_6) liquid scintillation detectors (volume of about 1 litre). These detectors, widely recognized [20] to be particularly suited for (n,γ) measurements, were further optimised [21] so as to have a very low sensitivity to background signals induced by sample-scattered neutrons (i. e. the amount of material constituting the detectors was minimised, and the materials used have a very low neutron capture cross-section). The detectors were placed face to face at 90° with respect to the beam and about 10 cm away from the sample.

The total energy detection principle was used by combining the detection system described above with the so called Pulse Height Weighting Technique (PHWT) [20, 22]. More details are presented in Sec. 3.2.

The data acquisition system consisted of 14 bit flash-ADC channels of TELEDYNE SP-Devices. These devices are equipped with an on-board memory of 512 MB per channel and can record digitised signals for 100 ms corresponding to all neutron energies down to 18 meV for EAR1. For the Gd measurement campaign, 4 channels for the C_6D_6 signals at a sampling rate of 1 GSample/s and 4 channels for the flux detectors with a sampling rate of 62.5 MSample/s were used.

2.3 Neutron flux

The procedure for the characterisation and definition of the neutron flux is described in detail in Ref. [23]. Its

evaluation results from a combination of dedicated measurements, performed with different detectors, based on neutron cross-section standards [24]. One of these detectors, the silicon monitor (SiMON) [25], was used during the measurement campaign to keep the neutron flux under systematic control. SiMON is based on the $^6\text{Li}(n,t)\alpha$ reaction standard and consists of a $600\text{ }\mu\text{g}/\text{cm}^2$ LiF foil placed on the beam, upstream with respect to the capture setup, viewed off-beam by 4 silicon detectors ($5\text{ cm}\times 5\text{ cm}\times 300\text{ }\mu\text{m}$). Such a configuration makes the SiMON apparatus almost transparent to neutrons. For instance, the applied correction for the presence of the LiF foil (accounting for the absorption of neutrons passing through it) is less than 1.4% for thermal neutrons. Moreover the reduction of the incoming neutron beam decreases with increasing neutron energy and becomes negligible (neutron transmission $> 99.5\%$) for neutron energies higher than 0.2 eV. Nevertheless, in the data analysis a correction for taking into account this effect was applied in the whole energy region of interest.

Fig. 1 shows a comparison of the energy distribution of the neutron flux impinging on the gadolinium sample, for a nominal proton bunch of 7×10^{12} protons, as extracted in 2014 and as measured in the present gadolinium campaign. The present flux was extracted using SiMON and is shown up to $E_n = 3\text{ keV}$, a region where no sizeable correction for non-isotropic emission of the reaction products is required. Above 1 eV the two curves agree within uncertainties, since the shape of the neutron flux is determined by the collimation system, which was not changed over the years. However, in the energy region below 1 eV, a systematic effect is clearly visible with a deviation reaching 9% near thermal energy. The magnitude and behaviour of this effect is linked to the change of the concentration of boric acid in the moderator circuit, which in 2016 increased by up to 7% with respect to 2014.

The 2016 neutron flux, with 100 bins per decade, has been determined within 1% uncertainty between thermal and 200 eV. The uncorrelated uncertainties, ascribed to counting statistics, start to play a major role at higher energies. Therefore, in order to avoid statistical fluctuations caused by the reduced statistics, the evaluated flux of 2014 was used above neutron energies of 200 eV.

Finally, a pick-up detection system based on the wall current monitor of the CERN Proton Synchrotron was used to monitor the proton current, which is proportional to the proton pulse intensity, and thus, to the neutron beam intensity.

2.4 Samples

The gadolinium samples were acquired from the National Isotope Development Center (NIDC) of the Oak Ridge National Laboratory (USA). Since the $^{155,157}\text{Gd}(n,\gamma)$ cross section changes by several orders of magnitude depending on the neutron energy, the measurement in the whole energy range could not be performed with a single sample. In particular, to avoid saturation of the capture yield attributable to self-shielding, very thin samples (3.2 and

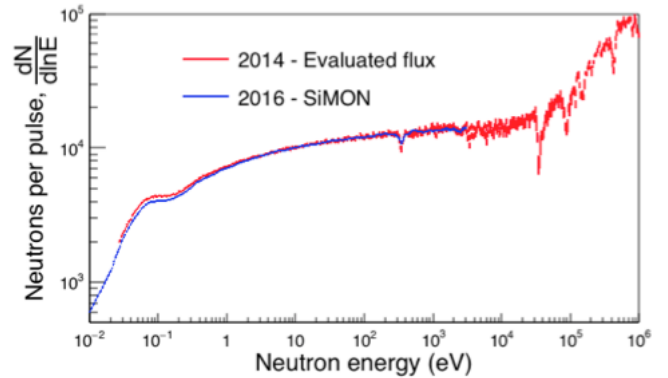


Fig. 1. (Color online) Neutron flux measured during the gadolinium campaign in the range 10 meV - 3 keV, compared to the flux evaluated in 2104.

$1.6\text{ mg}/\text{cm}^2$) were used to measure the cross sections near thermal-neutron energy. For the characterisation of resonant structures above 1 eV, 10- and 40-time thicker samples, for ^{155}Gd and ^{157}Gd , respectively, were used in order to obtain a good signal-to-background ratio in the resonance region. Hereafter, we will refer to these two sets of samples as to "thin" and "thick" gadolinium samples. The samples were isotopically enriched, with a cross contamination of other isotopes of less than 1.14%. In this way, possible background effects introduced by capture events in the contaminants were minimised. Table 2 summarises the characteristics of the samples, together with the declared uncertainties estimated from an isotopic analysis performed by the provider. The uncertainty on the areal density accounts for both uncertainties related to the weight and the area, which was determined to be less than 0.05% by an optical surface inspection with a microscope-based measurement system.

In addition to the 4 gadolinium samples, a ^{197}Au ($6.28 \times 10^{-4}\text{ at/b}$) and a lead sample ($6.71 \times 10^{-3}\text{ at/b}$) were used for normalisation and for the determination of the background. All the samples were circular in shape with a radius of 1 cm, in the form of self-sustaining metallic discs, thus avoiding possible background events induced by a sample container.

To prevent oxidation, the gadolinium samples were shipped in an airtight under-pressurised container. At the beginning of the experimental campaign the metal discs were extracted, weighted and sandwiched between two Mylar foils (thickness of $\approx 6\text{ }\mu\text{m}$) with a minimal amount of glue. An empty-sample was prepared, as a replica of the Gd samples, excluding the metal disc. Particular care was given to its production, similar to the gadolinium sample holder (i. e. an Al ring with 2 foils of mylar and a layer of glue).

3 Data analysis

The fraction of the neutron beam producing a neutron-capture reaction in the sample, namely the capture yield

Table 2. Features of the Gd samples with uncertainties declared by the provider.

Isotope	abundance %	% contamination of 155 or ^{157}Gd	% main contaminant	Weight mg	Areal Density atoms/barn $\times 10^{-8}$
^{155}Gd	91.74 ± 0.18	1.14 ± 0.01	5.12 ± 0.18 ^{156}Gd	100.6 ± 0.1	12440 ± 40
^{155}Gd	91.74 ± 0.18	1.14 ± 0.01	5.12 ± 0.18 ^{156}Gd	10.0 ± 0.1	1236 ± 12
^{157}Gd	88.32 ± 0.01	0.29 ± 0.01	9.10 ± 0.01 ^{158}Gd	191.6 ± 0.1	23390 ± 60
^{157}Gd	88.32 ± 0.01	0.29 ± 0.01	9.10 ± 0.01 ^{158}Gd	4.7 ± 0.1	574 ± 12

$Y(E_n)$, was obtained from the relation [20]

$$Y(E_n) = \frac{N}{S_n + E_n \frac{A}{A+1}} \frac{C_w(E_n) - B_w(E_n)}{\varphi_n(E_n) f_{BIF}(E_n)}. \quad (1)$$

Here, C_w is the weighted C_6D_6 counting rate for the Gd sample, N a normalisation factor independent of neutron energy, S_n the neutron separation energy of the compound nucleus, A the mass number of the target nucleus, B_w the weighted background count rate, φ_n the neutron fluence and f_{BIF} is a correction factor taking into account the variation of the neutron-beam interception as a function of the neutron energy. In the following sections a detailed explanation of the data reduction procedure is addressed, with particular care to the correction factors (Secs. 3.2, 3.3 and 3.5) which determine the final uncertainty. The study of the stability of the detectors, their calibration and the time-of-flight to neutron energy conversion are also discussed in sections 3.1 and 3.4.

3.1 Detector resolution and calibration

With the aim of obtaining high accuracy cross section data, the experimental setup has been carefully characterised, with particular reference to the stability and the performance of the detectors. The stability of the detector response, mostly related to the gain of the photomultipliers, has regularly been verified by measurements with standard γ -ray sources, namely ^{137}Cs ($E_\gamma = 0.662$ MeV), ^{88}Y ($E_\gamma = 0.898$ MeV and $E_\gamma = 1.836$ MeV), and the composite Am-Be ($E_\gamma = 4.44$ MeV) and Cm-C ($E_\gamma = 6.13$ MeV) sources (see Fig. 2). The energy spectra of γ -ray sources were recorded more than once per week and did not reveal a gain shift higher than 0.7%, as can be seen in the inset of Fig. 2 obtained with the Yttrium source.

A reliable calibration of the detectors is an important aspect of the data analysis, because of the (possible) modification of the detector response, to be used in the application of the PHWT. The calculation of the weighting factors, indeed, depends on the discrimination level applied to the deposited energy spectra. For this reason, particular care was taken to determine the experimental resolution as a function of γ -ray energy and energy calibration of the detectors. The iterative procedure followed to achieve this objective consisted of (i) extraction of the energy resolution from experimental spectra acquired with standard γ -ray sources; (ii) broadening of the simulated spectra with the energy resolution so as to reproduce the measurements

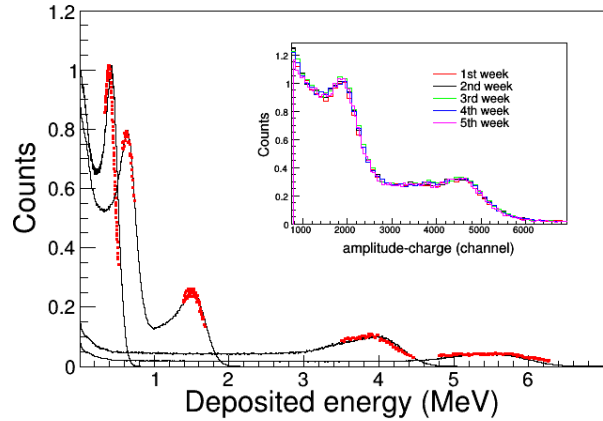


Fig. 2. Calibrated amplitude spectra for ^{137}Cs , ^{88}Y , Am-Be and Cm-C standard γ -ray sources. The black lines correspond to the simulated spectra, convoluted with the energy resolution, while the red dots are experimental data. The inset shows various ^{88}Y spectra taken during the gadolinium experimental campaign.

(as shown in Figure 2); (iii) fine calibration of the detectors, determined by the best matching between simulated and measured spectra.

3.2 Determination of weighting functions

The total-energy detection principle was applied, combining low efficiency detection system, such as the present setup based on C_6D_6 detectors, with the pulse height weighting technique (see Ref. [20] and [22] and references therein) in order to assure the proportionality between the detection efficiency to the corresponding γ -ray energy. The proportionality is achieved by introducing a mathematical procedure based on a weighting function $WF(E_d)$, E_d being the energy deposited by a γ ray. The description of the detection system response was determined using a Monte Carlo simulation of the apparatus, by GEANT4 simulation [26] of the complete experimental assembly. The response of the detection system has been studied as a function of the γ -ray energy. In the MC simulation, the γ rays were emitted from the sample according to the Gaussian xy distribution of the neutron beam profile, uniformly in z direction with z axis being the direction of the neutron beam. Then, the final detector response was obtained by convoluting the simulated response with a Gaussian

function that represents the detector resolution. The γ -ray transport in the sample can play a relevant role for the thick samples and, generally, for high values of the product $n\sigma_{tot}$, where n is the areal density in atoms/barn and σ_{tot} is the total cross section. The case of a spatial distribution with exponential shape along z for the emitted γ ray in the sample was evaluated and is discussed in Sec. 3.6.

The weighting function $WF(E_d)$ was parameterised with a polynomial function by minimising the difference between the weighted response and the corresponding γ -ray energy for a number of energies in the range of interest. The discrimination level was fixed to 150 keV and the upper threshold to 10.0 MeV, corresponding to the Compton edge of γ -ray energies of 285 keV and 10.3 MeV, respectively. The upper threshold exceeds the neutron separation energies of ^{156}Gd ($S_n = 8.54$ MeV), ^{158}Gd ($S_n = 7.94$ MeV) and ^{198}Au ($S_n = 6.51$ MeV) to take into account the resolution broadening of the scintillation detectors. The impact of these analysis conditions on the uncertainty related to the PHWT is discussed in Sec. 3.6.

The loss of cascade γ -rays attributable to the electron conversion process should be considered for a careful estimation of the uncertainty related to the PHWT. The Monte-Carlo DICEBOX algorithm [27] was used to produce artificial capture cascades and estimate this effect. In DICEBOX, the complete decay scheme is taken from existing experimental data below a certain critical energy, E_{crit} . The data from Refs. [28], [29] and [30] for $^{156,158}\text{Gd}$ and ^{198}Au , respectively, were used and the value of E_{crit} was adjusted for each isotope to ensure the completeness of the decay scheme. Above E_{crit} the statistical model, in terms of level density (LD) and a set of photon strength functions (PSFs) for different transition types, was adopted to generate individual levels and their decay properties. The LD and PSFs models and their parameters were taken from Refs. [31], [32] and [33] for $^{156,158}\text{Gd}$ and ^{198}Au , respectively. DICEBOX computes the contribution of internal electron conversion using parameters from the BrIcc database [34] for all transitions above E_{crit} and for those transitions below E_{crit} where the experimental information about internal electron conversion is lacking.

The generated cascades were used as input to the GEANT4 simulation described above. The comparison between the experimental spectrum from $^{155}\text{Gd}(n,\gamma)$ near thermal point with the simulated one is shown in Fig. 3. Several different artificial nuclei were produced with the DICEBOX code to mimic the uncertainty in the decay scheme. The three red curves, corresponding to the average value and this value \pm standard deviation from simulations of different artificial nuclei, indicate the expected uncertainty due to the statistical nature of the decay process. The influence of differences between Gd and Au cascades is discussed in Sec. 3.6.

3.3 Background subtraction

The study of the background in the capture data, B_w in Eq. (1), is based on dedicated measurements aimed at

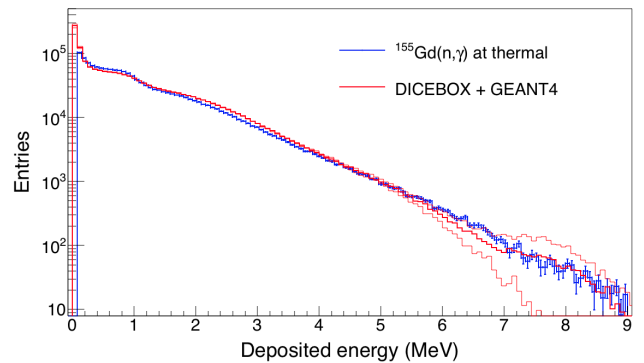


Fig. 3. (Color online) C_6D_6 energy spectrum for $^{155}\text{Gd}(n,\gamma)$ at neutron energy near thermal compared to the simulated response. The red curves represent the average value and the expected uncertainty.

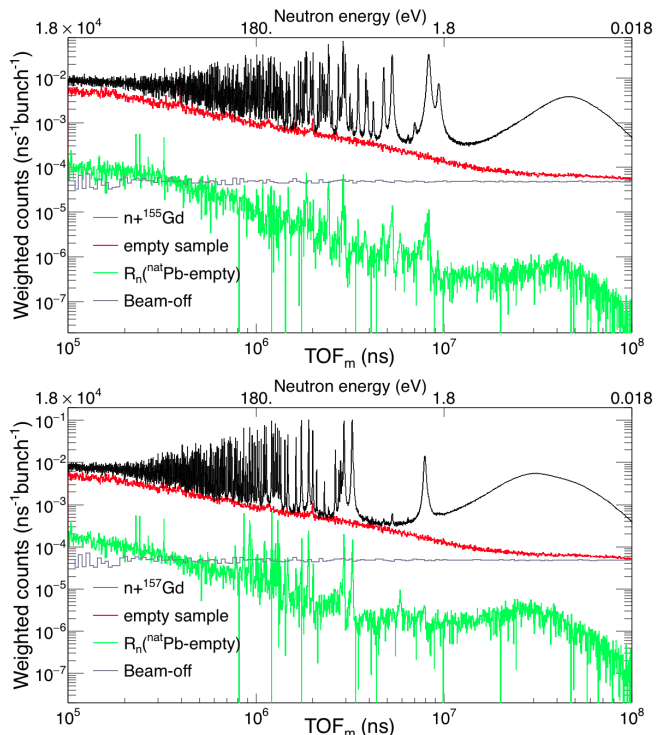


Fig. 4. (Color online) Weighted C_6D_6 time-of-flight spectrum of the thick ^{155}Gd sample (top) and the thick ^{157}Gd sample (bottom), together with background measurements.

evaluating the various components which can be ascribed to: (i) neutron beam interactions with anything but the sample, (ii) sample-scattered neutrons, (iii) γ rays traveling in the beam and (iv) time-independent background. In Fig. 4 the measured time-of-flight (TOF_m) spectra, used to estimate these background components, are shown together with the TOF_m spectrum for both thick $^{155,157}\text{Gd}$ samples for comparison. The first background component has been evaluated with a measurement of the empty-sample holder (Sec. 2.4) in the beam, thus accounting for any beam-related effect not linked to the presence of a sample. The second source of background is due to γ rays

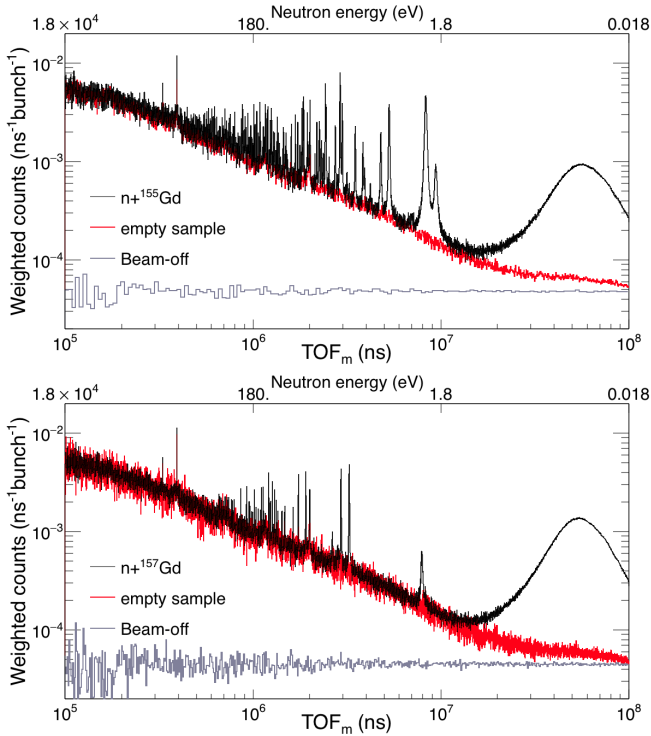


Fig. 5. (Color online) Weighted C_6D_6 time-of-flight spectrum of the thin ^{155}Gd sample (top) and the thin ^{157}Gd sample (bottom), together with background measurements.

originating from sample-scattered neutrons, thermalised and captured in the surrounding materials. This component was evaluated with a measurement of a lead sample, placed in the beam. The counts of the empty-sample measurement, normalised to the same neutron intensity, were subtracted from the Pb measurement and a correction factor, R_n , was applied to the resulting quantity. R_n is the ratio of the neutron scattering yield of Gd and Pb samples. The third background component, mainly 2.2 MeV and 0.48 MeV in-beam γ rays from neutron capture in the Hydrogen and Boron of the moderator, respectively, was estimated by the measurement with the lead sample as well. This kind of background starts to contribute in the energy region above 300 eV ($\text{TOF}_m \lesssim 7.7 \times 10^5$ ns). Its time distribution results from the combination of the neutron slowing-down process in the moderator and the flight-path length. The fourth background component, related to ambient radioactivity and activation of the materials inside the experimental area, was estimated with a beam-off measurement. Since the products of $^{155}\text{Gd}(n,\gamma)$ and $^{157}\text{Gd}(n,\gamma)$ are the stable ^{156}Gd and ^{158}Gd isotopes, a background due to the activation of the sample is negligible.

Fig. 5 shows the C_6D_6 background measurements compared with the signals resulting from the measurement with the thin ^{155}Gd and ^{157}Gd samples. In this case the neutron background is not shown to highlight the comparison between the Gd and the empty measurement. As expected, the signal-to-background ratio is much less favourable for instance at 2 eV it is about 200 and 30 for thick and

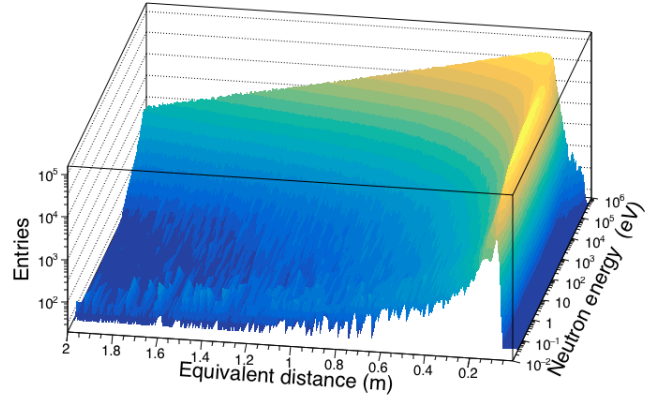


Fig. 6. (Color online) Distribution of $\lambda(E_n)$ as a function of neutron energy.

thin samples, respectively. The figure also shows the expected matching between resonance valleys and the empty-sample measurement.

In summary, the empty-sample measurement satisfactorily represents the background level in the energy range of interest. A similar evaluation was repeated for the thin and thick $^{157}\text{Gd}(n,\gamma)$ measurement and resulted in the same conclusion. It is worth mentioning that at thermal-neutron energy ($\text{TOF}_m \approx 85 \times 10^6$ ns) the signal-to-background ratio for the thin gadolinium samples was 7.7 and 10 for ^{155}Gd and ^{157}Gd , respectively.

3.4 Time-of-flight to energy calibration

At n_TOF, the neutron kinetic energy is calculated from the velocity of the neutrons. The latter quantity cannot be directly derived from the ratio of the geometrical flight-path length L_0 to the measured TOF_m , because TOF_m also depends on the moderation time (i. e. the time spent by the neutron inside the target assembly). This case was discussed in more details in Refs. [18] and [19], here we only remind the reader that it is customary to express the distribution of the moderation time in terms of an equivalent distance $\lambda(E_n)$, which depends on the neutron energy. Consequently, the effective flight path $L(E_n)$ is the sum of a time independent term L_0 and a time dependent term, which is given by the average value of the $\lambda(E_n)$ distribution: $L(E_n) = L_0 + \langle \lambda(E_n) \rangle$. Fig. 6 shows the $\lambda(E_n)$ distribution obtained by Monte Carlo simulations [35,36]; it is worth noticing that the average of the distribution, 19 cm, varies only slightly with the neutron energy. Therefore, the kinetic energy can be extracted with a recursive procedure which converged after a few iterations. The value of $L_0 = 183.92(8)$ m resulted from a minimisation procedure adopting the well-known low-energy resonances of ^{197}Au retrieved from JEFF-3.3 evaluation [37]. This geometrical (i. e. energy independent) value, obtained with the least square adjustment, is consistent with the design value of 183.94 m.

3.5 Normalisation and Beam Interception Factor

The normalisation factor, N in Eq. (1), groups together the correction factors independent of neutron energy: efficiency related to the solid angle of the detectors, fraction of the neutron beam intercepting the gadolinium sample (0.68 is the nominal value [18]) and the absolute value of the neutron flux. This normalisation coefficient was obtained by the saturated resonance technique [38,20], applied to the 4.9 eV resonance in $n+^{197}\text{Au}$. The Au capture yield was analysed with the R-Matrix code SAMMY [39] and the value of the normalisation was extracted with an uncertainty due to counting statistic of less than 0.1%. The impact of the systematic effects related to the difference of the electromagnetic cascade for $^{197}\text{Au}(n,\gamma)$ and $^{155,157}\text{Gd}(n,\gamma)$ is discussed in Sec. 3.6.

The beam interception factor (i. e. the fraction of the neutron beam intercepting the sample) can be considered constant within less than 1.5% variation in the energy region between $E_n = 1$ eV and 100 keV [18]. As thoroughly discussed in Refs. [18,19], the beam profile has a Gaussian distribution with standard deviation of about 6 mm, determined mainly by the collimation system. Below 1 eV, Monte Carlo simulations and previous n.TOF experiments have demonstrated that a correction factor, f_{BIF} in Eq. (1), is required for taking into account the modification of the spatial distribution of the beam profile. Unfortunately, the correction is extremely sensitive to small changes in the collimation system, which cannot be fully controlled and therefore accurately implemented in MC simulations. In addition, the gravitational force plays a sizeable role at very low energies, because the vertical displacement of neutrons of 25 meV is 3.5 cm, after traveling for 185 m. Consequently, only qualitative information could be drawn from Monte Carlo simulations, as the beam profile becomes larger and asymmetric as the neutron energy decreases and the expected uncertainty on the related correction factors can be as high as 20%.

In the present analysis, an empirical method was used for the correction of the beam interception factor. It is similar to the saturated resonance technique, i. e. the product of the areal density and cross section is high enough for all incident neutrons to interact with the sample. The expected capture yield can be expressed as [20]:

$$Y(E_n) = (1 - e^{-n\sigma_{tot}(E_n)}) \frac{\sigma_\gamma(E_n)}{\sigma_{tot}(E_n)} + Y_M, \quad (2)$$

where n is the areal density of the sample (reported in Table 2), σ_{tot} is the total cross section, σ_γ is the capture cross section and Y_M accounts for the contribution of capture events following at least one neutron scattering in the sample (see Ref. [20] for more details). In the case of the thick ^{155}Gd and ^{157}Gd samples, $n\sigma_{tot}(E_n)$ is so high that the calculated transmission of neutrons through the samples is less than 10^{-3} , for neutron energies below 0.07 and 0.1 eV, respectively. Considering also that the ratio of elastic to capture cross section is less than 10^{-2} in this energy region, the capture yield for thick gadolinium samples is expected to be $Y = 1$. Any departure of the measured

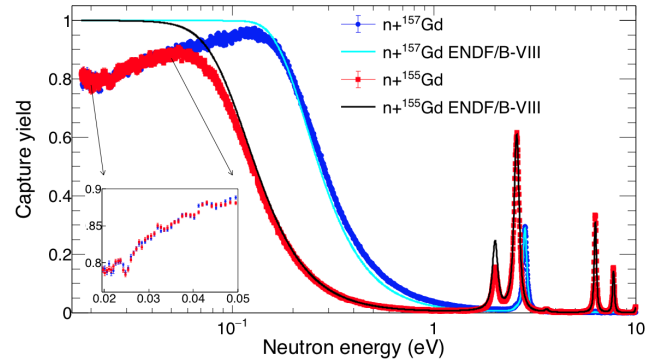


Fig. 7. (Color online) Capture yield of the thick gadolinium samples measured in this work and comparison with the expected capture yield calculated on the basis of the cross sections in ENDF/B-VIII.0 library. The region between $E_n = 0.02$ and 0.05 eV, linked to the correction for the variation of the beam interception factor, is shown in the inset.

capture yield from unity can be ascribed to a variation of the beam intercepting the sample. The situation is illustrated in Fig. 7 where the experimental $^{155}\text{Gd}(n,\gamma)$ and $^{157}\text{Gd}(n,\gamma)$ capture yields are compared to their expected values of Eq. (2), calculated with the resonance parameters contained in the ENDF/B-VIII.0 evaluation. In the inset of the figure, the energy region where the empirical f_{BIF} was extracted is highlighted. The two sets of data are very similar, confirming the presence of a common effect.

The empirical correction factor was used to correct the capture yields of the thin gadolinium and gold samples, as discussed in the next section.

3.6 Quality assessment and discussion on uncertainties

As mentioned above, one of the aims of this measurement was to estimate the cross section at thermal energy for ^{155}Gd and ^{157}Gd . In this region, the uncorrelated uncertainties have a minor role, since the involved cross sections are very high and consequently the counting statistics does not contribute. On the contrary, correlated uncertainties dominate the total uncertainty. They come from the normalisation, PHWT, background determination and subtraction, sample characterisation and neutron flux shape. In addition, in the energy region below 1 eV the uncertainty due to correction for the beam interception factor needs to be considered as explained in the previous section. In Table 3 the different contributions are listed together with the total uncertainty for both gadolinium isotopes in the thermal region and in the resonance region. In the latter region also the uncertainty on the temperature has an impact, since it modifies the profile of the resonances. Hereafter each component is discussed separately.

The uncertainty related to the normalisation depends on the difference between the electromagnetic cascades in $^{197}\text{Au}(n,\gamma)$ and in $^{155,157}\text{Gd}(n,\gamma)$. One component of this effect is due to electron conversion, while a second component can be ascribed to γ rays missed because of the

discrimination level set in the detectors. To quantify such a bias, the method adopted in Ref. [40] was applied. The count losses attributable to the detector threshold were estimated by means of simulated cascades (described above, in Sec. 3.2). The weighted contribution of missed γ rays with energies below the threshold and those of electrons are 1.0% and 0.8% respectively, for ^{198}Au . Meanwhile, for both ^{156}Gd and ^{158}Gd , the weighted contributions are similar, with values of 0.4% for missing γ rays and 0.2% for conversion electrons. Therefore, the bias in the normalisation due to the detector threshold is 0.6% for missing γ rays and 0.6% for conversion electrons. Since these are model-dependent corrections (which depend also on the detector performances), they were added up to evaluate an uncertainty on the normalisation which was estimated to be 1.2%.

The uncertainty related to the weighting function was investigated by repeating the data analysis by using: i) linear and quadratic amplitude to deposited energy calibration; ii) detector threshold of 150, 175 and 200 keV and corresponding weighting functions; iii) 7 different weighting functions calculated with an exponential attenuation in the direction of the neutron beam according to different values of $n\sigma_{\text{tot}}$. For all these cases, the ratio between the experimental yields never changed by more than 1.5%. Moreover, systematic effects due to the positioning of the sample with respect to the detection system and the neutron beam were minimised. In particular samples were centred using a micrometric positioning system based on a jig and a hollow metallic cylinder aligned with the Al annular frame.

The uncertainty component related to the background subtraction propagates into the total uncertainty according to the signal-to-background ratio. From measurements using different empty samples, and from the comparison of the TOF spectra measured with the empty sample and the thin gadolinium samples (between resonances), we deduced an uncertainty of 10%. Therefore, at thermal neutron energy the uncertainty attributable to the background subtraction is 1.4% for ^{155}Gd and 1.0% for ^{157}Gd (the signal-to-background ratio is 7.7 and 10, respectively), whereas in the resonance region it depends on the resonance strength.

The uncertainty on the correction of the beam interception factor was estimated by analysing the capture yield of $^{197}\text{Au}(n,\gamma)$, since its cross section is a standard at thermal energy [24]. In addition the cross section near thermal energy is characterised by the $1/v$ behaviour and therefore the knowledge of the capture yield at thermal energy constrains the shape of the capture yield at higher energies as well. In Fig. 8 two experimental $^{197}\text{Au}(n,\gamma)$ capture yields are shown together with the expected capture yield based on the JEFF-3.3 evaluation [37]. The two data sets differ by applying the correction for the beam interception factor. Near thermal energy (highlighted in the inset of the figure) the expected capture yield is well reproduced when the correction is applied and the corresponding thermal cross section is 98.5(34) b. In particular, the average ratio between the corrected data and the ex-

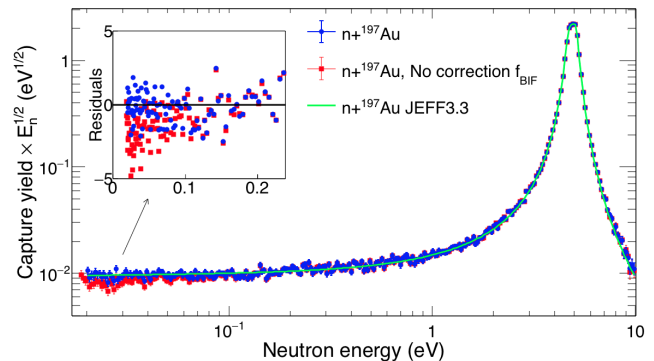


Fig. 8. (Color online) $^{197}\text{Au}(n,\gamma)$ capture yields (multiplied by $E_n^{1/2}$) with and without the correction for the variation of the beam interception factor and comparison with the expected capture yield calculated on the basis of the cross sections in JEFF-3.3 library.

pected capture yield is 0.985 in the region $0.02 \leq E_n \leq 0.1$ eV. Based on this we adopted the uncertainty of 1.5% for the beam interception factor.

For the estimation of the uncertainty of the shape of the neutron flux, we adopted an uncertainty of 1% as discussed in [23,118].

Very thin samples can suffer from inhomogeneity because of the preparation procedure. R-matrix codes such as CONRAD [41] and REFIT [42] can take into account this effect and propagate the uncertainty to the extracted cross section, as explained in ref. [20]. In this case, in order to constrain the possibly large uncertainty claimed by the provider (uniformity better than 10%), we have compared the results of the resonance shape analysis for strong resonances as observed in the capture yields of thin and thick samples, see Secs. 4.1 and 4.2 for details. For both pairs of samples the results were consistent within 2%, hence the uncertainty in the uniformity can be accounted for as a part of the sample mass uncertainty. This comparison was also the confirmation that the uncertainties summarised in Table 3 can be considered as the full uncertainty of the present measurements.

4 Resonance shape Analysis

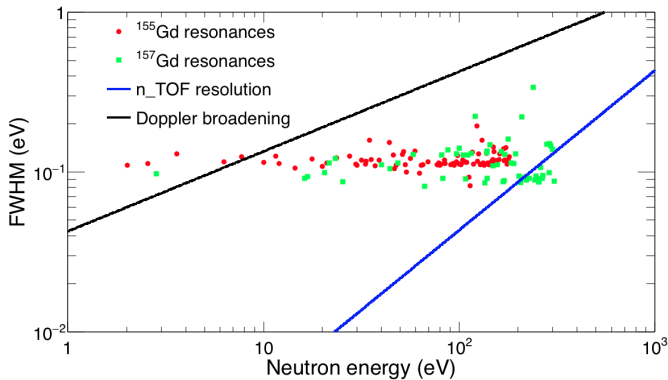
The capture yields were analyzed with the R-Matrix analysis code SAMMY, using the Reich-Moore approximation. Corrections for experimental conditions such as Doppler and experimental broadening, self-shielding and multiple neutron interactions in the sample (i. e. multiple scattering) were taken into account by the code. In particular, the response of the spectrometer (shown in Fig. 6) was implemented in SAMMY by using the user-defined resolution function option: i. e. a numerical description derived from a Monte Carlo simulations. The thermal motion of gadolinium atoms inside the sample was taken into account by means of the free-gas model with a temperature of 296(1) K, as monitored during the experiment. The corresponding effective temperature used in the RSA was

Table 3. Summary of the correlated uncertainties in the $^{155}\text{Gd}(n,\gamma)$ and $^{157}\text{Gd}(n,\gamma)$ cross section measurements.

Source of uncertainty	$^{155}\text{Gd}(n,\gamma)$		$^{157}\text{Gd}(n,\gamma)$	
	near thermal	resonance region	near thermal	resonance region
Normalization	1.2%	1.2%	1.2%	1.2%
PHWT	1.5%	1.5%	1.5%	1.5%
Background	1.4%	$\approx 1\%$	1.0%	$\approx 1\%$
BIF	1.5%		1.5%	
Flux	1.0%	1.0%	1.0%	1.0%
Sample mass	1.0%	$< 0.2\%$	2.1%	$< 0.2\%$
Temperature		1%		1%
Total	3.2%	2.6%	3.5%	2.6%

301(1) K and its uncertainty was taken into account in the resonance shape analysis (RSA).

The resonance parameters and the scattering radius from the ENDF/B-VIII.0 library were adopted as the initial values of a fitting procedure. The scattering radius as well as the spin and parity of the resonances were not changed, because the capture data are not sensitive enough to these quantities. As showed in Fig. 9, where the total resonance width of the gadolinium resonances are compared to the different contributions to the actually observed broadening, the Doppler effect is larger than the resonance width for $E_n \gtrsim 10$ eV and starts to limit the RSA sensitivity to the total width (and therefore Γ_γ). Nevertheless, in the analysis the resonance energy and both Γ_n and Γ_γ were varied because the χ^2 value of fit was smaller with respect to the case where only Γ_n was allowed to vary and Γ_γ was fixed to the average value.

**Fig. 9.** Resonance widths compared to experimental broadenings.

Since the spin assignments in the evaluations are sometimes inconsistent and do not take into account recent results [17], the value of $g\Gamma_n$ (g is the statistical spin factor) is reported in this work, because its value is independent of the spin of the resonance. In the RSA, the presence of contaminant Gd isotopes in the sample was taken into account. In particular, the resonance parameters from the ENDF/B-VIII.0 evaluation were used and kept fixed.

The resolved resonance regions (RRR) in nuclear data libraries such as ENDF/B-VIII.0, JEFF-3.3 and JENDL-4.0 are limited to the energy region below 307 eV for $n+^{157}\text{Gd}$ and below 181 eV for $n+^{155}\text{Gd}$. The present data clearly show structures well above these energies (see Fig. 18 in Appendix A.1). These structures have been analysed assuming they are s -wave resonances with an average Γ_γ deduced from the resonances in the RRR. Their energy and capture kernel, defined as $g\Gamma_\gamma\Gamma_n/(\Gamma_\gamma + \Gamma_n)$ are reported in Appendix A.1. In order to extend the resolved resonance region to higher energies, it would be necessary to perform a transmission experiment on the same thick samples.

For energies below 0.5 eV, only the data obtained with the thin samples were used. A simultaneous resonance shape analysis of data obtained with both, thin and thick samples, was performed up to 5 eV. Above this energy, only the data obtained with the thick samples were used. Nevertheless, as already mentioned above, a few strong resonances in the energy region up to 60 eV were used to cross-check the capture data obtained with the thin samples, see Table 4 for details.

The results of the resonance shape analysis were used to reconstruct the cross section and in particular to evaluate the thermal cross section $\sigma_0 = \sigma_\gamma(E_0)$ at $E_0 = 0.0253$ eV. In addition, the cross section reconstructed using the resonance parameters from this work has been convoluted with a Maxwellian neutron energy distribution to obtain the so called Maxwellian averaged cross section:

$$\frac{2}{\sqrt{\pi}} \frac{\int \sigma_\gamma(E_n) E_n e^{-E_n/E_0} dE_n}{\int E_n e^{-E_n/E_0} dE_n}. \quad (3)$$

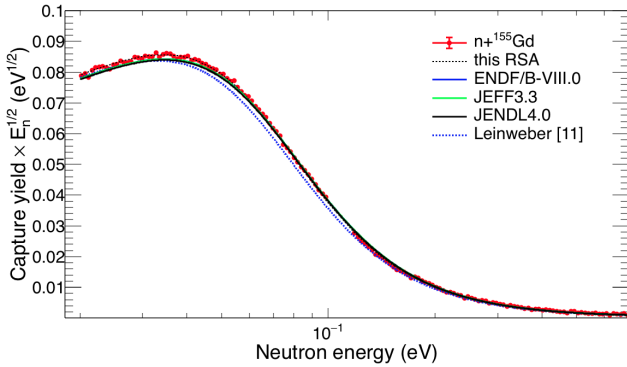
The ratio of the latter quantity for thermal energy $E_0 = 0.0253$ eV to σ_0 , referred to as the Westcott factor [8], was also calculated. It allowed us to evaluate the non- $1/v$ behaviour of the capture cross section (i. e. the Westcott factor significantly different from unity).

4.1 $n+^{155}\text{Gd}$

The capture cross section of ^{155}Gd at thermal energy does not vary significantly among libraries. It ranges from 60.735

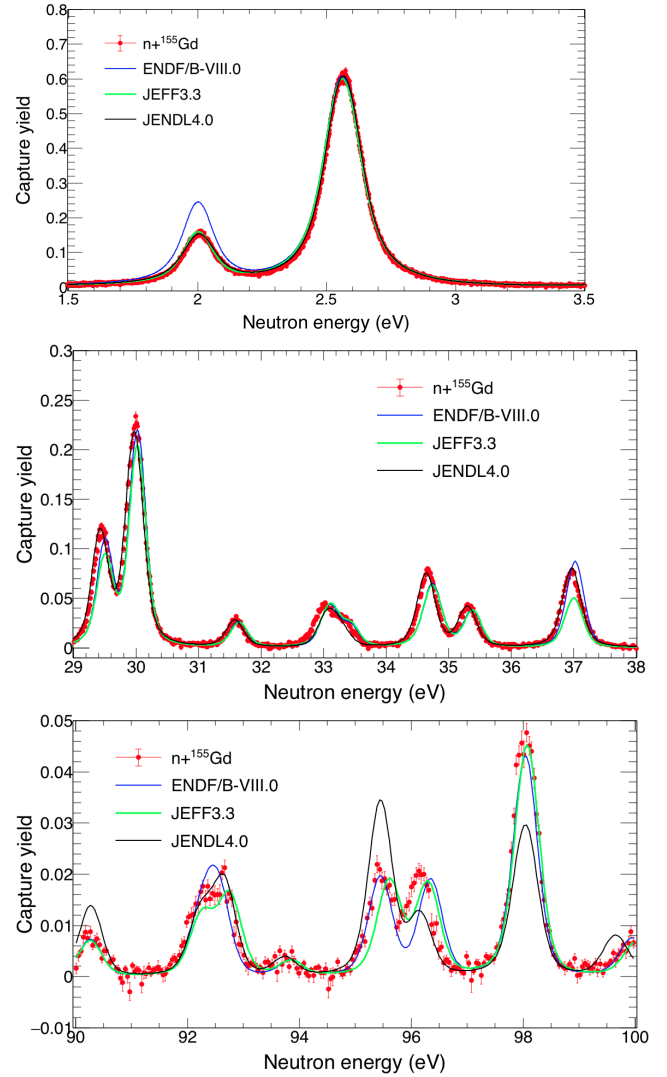
Table 4. $^{155}\text{Gd}(n,\gamma)$ and $^{157}\text{Gd}(n,\gamma)$ resonance kernels resulting from thin and thick samples, used for testing the homogeneity of the thin samples, see text for details.

Resonance energy (eV)	capture kernel (meV) thick sample	thin sample	Ratio
$^{155}\text{Gd}(n,\gamma)$			
2.5730	1.021(1)	1.036(10)	0.99(1)
6.3062	1.305(3)	1.304(12)	1.00(2)
7.7490	0.694(3)	0.697(12)	1.00(2)
19.8790	2.65(1)	2.7(2)	0.98(8)
20.9902	6.61(2)	6.7(9)	0.98(14)
30.0702	6.27(3)	6.33(11)	0.99(14)
43.868	5.71(5)	5.6(7)	1.02(15)
51.290	6.65(6)	6.8(9)	0.98(15)
52.041	6.41(6)	6.3(8)	1.01(15)
$^{157}\text{Gd}(n,\gamma)$			
2.8329	0.2286(4)	0.225(5)	1.01(2)
16.7946	7.685(1)	7.649(10)	1.00(1)
20.5262	7.45(2)	7.471(12)	1.00(2)
44.1374	5.45(2)	5.3(3)	1.02(6)
48.7076	13.52(4)	13.3(5)	1.02(4)
58.2927	15.39(5)	15.0(7)	1.02(5)

**Fig. 10.** (Color online) $^{155}\text{Gd}(n,\gamma)$ capture yield (multiplied by $E_n^{1/2}$) from the thin sample compared with the expected capture yields calculated on the basis of the cross sections in ENDF/B-VIII.0, JEFF-3.3 and JENDL-4.0 libraries and resonance parameters in Ref. [11].

to 60.890 kb. In Figure 10 the present capture yield, obtained with the thin sample, is compared with the expected capture yields calculated from the resonance parameters in evaluations and Ref. [11]. From the present data a slightly higher but consistent thermal cross section was deduced, $\sigma_0 = 62.2(2.2)$ kb. The resulting Westcott factor is 0.86(4).

In the resolved resonance region, differences are present in evaluated nuclear data files. Moreover, two relatively recent time-of-flight measurements present inconsistencies. In particular, for a number of resonances, the measurement of Leinweber and collaborators [11] sizeably disagrees with the ENDF/B-VIII.0, while the measurement by Baramsai and collaborators [17] tends to confirm the resonance parameters in ENDF/B-VIII.0.

**Fig. 11.** (Color online) $^{155}\text{Gd}(n,\gamma)$ capture yield obtained with the thick target compared to the expected capture yields, calculated on the basis of the cross sections in ENDF/B-VIII.0, JEFF-3.3 and JENDL-4.0 nuclear data libraries.

Examples of some of the largest differences between the present data and the evaluations are shown in Fig. 11. For instance, our capture kernel of the resonance at 2.0 eV is about 50% lower than the value calculated from ENDF/B-VIII.0. Large deviations with respect to JENDL-4.0 are present as well, as for example in the case of the resonances at 95.7 eV and 98.3 eV. Fig. 11 shows the good energy resolution of the present data, which enabled us to resolve some doublets, such as the structures at $E_n = 33$, 93 or 96 eV. The presence of small structures at 43.43, 54.81, 62.12, 68.98 and 76.19 eV reported in JEFF-3.3 and 17.81 and 68.81 eV reported by Baramsai and collaborators [17], cannot be excluded or confirmed on the basis of present data since they are overwhelmed by the background. It cannot be excluded that some weak resonances, as for example the one at 22.45 eV in Ref. [17] could be attributable to multiple scattering in the nearby

resonances rather than a genuine resonance as quoted in ENDF/B-VIII (see for instance Fig. 21 in Ref. [43] about this possible effect). Finally, the resonance reported by Leinweber and collaborators at $E_n = 131.7$ eV is also observed in the present measurement at $E_n = 131.35$ eV.

The results of the resonance shape analysis are summarised in Table 5. The correlation coefficient between partial widths $\rho(\Gamma_\gamma, \Gamma_n)$ resulting from the SAMMY fit is also reported.

Table 5: Resonances in $^{155}\text{Gd}(n,\gamma)$. Uncertainties are from the fit. Partial widths are reported for information, capture kernels being the experimental quantity of interest. In bold the doubtful resonance at 37.28 eV.

Energy (eV)	Γ_γ (meV)	$g\Gamma_n$ (meV)	$\rho(\Gamma_\gamma, \Gamma_n)$	capture kernel (meV)
0.0268	104.57(8)	0.0644(5)	0.48	0.0643(5)
2.0128(2)	111.0(6)	0.1350(4)	0.47	0.1346(4)
2.5730(1)	102.8(2)	1.037(1)	-0.17	1.021(1)
3.618(2)	125(7)	0.0141(4)	0.71	0.0143(4)
6.3062(2)	103.6(5)	1.332(3)	0.08	1.305(3)
7.7490(4)	102.3(8)	0.698(3)	0.34	0.690(3)
10.000(2)	102(5)	0.107(2)	0.65	0.107(2)
11.507(1)	105(4)	0.219(3)	0.64	0.218(3)
11.9729(7)	107(2)	0.653(4)	0.54	0.646(4)
14.4851(6)	102(1)	1.238(6)	0.29	1.199(6)
17.733(2)	97(7)	0.240(5)	0.62	0.238(5)
19.8790(6)	107(1)	2.76(1)	0.25	2.65(1)
20.9902(4)	121(1)	7.25(2)	-0.12	6.61(2)
23.626(1)	94(6)	1.49(2)	0.36	1.45(1)
27.519(3)	101(8)	0.405(9)	0.66	0.409(8)
29.528(1)	112(3)	2.96(3)	0.59	2.84(3)
30.0702(7)	108(2)	6.91(3)	0.31	6.26(3)
31.674(3)	96(7)	0.68(1)	0.28	0.66(1)
33.047(3)	130(10)	0.90(2)	0.76	0.89(2)
33.464(5)	70(20)	0.49(2)	0.79	0.48(2)
34.758(1)	114(4)	2.47(2)	0.43	2.34(2)
35.408(2)	107(7)	1.21(2)	0.64	1.19(2)
37.046(5)	109(9)	2.59(1)	0.81	2.44(1)
37.28(2)	80(50)	0.31(1)	0.77	0.31(1)
38.937(2)	103(10)	0.65(2)	0.60	0.64(1)
43.868(1)	117(5)	6.56(6)	-0.13	5.71(4)
46.006(3)	126(10)	1.36(4)	0.62	1.33(3)
46.806(2)	97(5)	3.46(4)	0.45	3.27(3)
47.64(1)	80(30)	0.21(2)	0.60	0.21(1)
51.290(2)	138(5)	7.62(7)	0.15	6.51(6)
52.041(1)	97(5)	7.79(7)	-13	6.41(6)
52.918(7)	120(20)	0.86(5)	0.80	0.85(3)
53.639(2)	97(5)	5.11(5)	0.26	4.71(4)
56.130(4)	110(12)	1.38(3)	0.52	1.35(3)
59.321(2)	108(6)	4.21(5)	0.28	3.95(4)
62.751(2)	129(6)	4.88(6)	0.23	4.59(5)
64.06(3)	109	0.17(2)		0.17(2)
65.17(2)	109	0.34(2)		0.36(2)
69.459(3)	120(10)	3.77(6)	0.55	3.60(5)
76.835(8)	100(20)	0.99(4)	0.68	0.97(3)
77.60(2)	90(40)	0.39(2)	0.64	0.38(2)
78.761(7)	112(12)	2.67(5)	0.06	2.57(5)

Continued

Table 5 (Continued)

Energy (eV)	Γ_γ (meV)	$g\Gamma_n$ (meV)	$\rho(\Gamma_\gamma, \Gamma_n)$	capture ker (meV)
78.9(2)	109	0.10(2)		0.095(9)
80.70(1)	90(30)	0.83(3)	0.59	0.81(3)
83.980(4)	91(11)	3.63(7)	0.11	3.29(6)
84.916(9)	120(20)	1.27(4)	0.62	1.24(4)
90.53(1)	120(30)	0.80(4)	0.63	0.79(3)
92.44(1)	100(30)	1.55(8)	0.74	1.51(7)
92.89(1)	70(30)	1.79(8)	0.73	1.72(7)
93.94(3)	120(50)	0.36(2)	0.47	0.35(2)
95.710(8)	110(30)	2.40(7)	0.45	2.32(7)
96.403(9)	100(30)	2.47(8)	0.61	2.32(7)
98.302(4)	80(9)	7.6(2)	-0.74	6.06(9)
100.21(2)	160(50)	0.81(6)	0.56	0.80(4)
101.35(1)	100(40)	1.38(5)	0.78	1.38(5)
101.99(2)	80(40)	0.87(4)	0.60	0.84(4)
104.413(7)	100(20)	3.33(8)	0.11	3.08(8)
105.942(8)	110(20)	2.42(8)	0.35	2.29(7)
107.118(6)	110(20)	4.01(8)	0.49	3.79(8)
109.55(1)	100(30)	1.63(6)	0.39	1.56(6)
112.389(5)	100(10)	5.54(2)	0.12	5.12(9)
113.822(3)	126(8)	11.2(1)	-0.19	9.9(1)
116.541(5)	122(13)	7.8(1)	-0.33	6.7(1)
118.69(2)	90(30)	1.18(6)	0.37	1.16(6)
123.377(4)	100(20)	16.7(3)	-0.95	11.54(2)
124.448(8)	60(20)	4.1(1)	0.24	3.7(1)
126.102(5)	120(10)	9.3(2)	-0.42	7.7(1)
128.55(6)	80(40)	0.44(8)	0.04	0.45(3)
129.73(4)	80(40)	1.53(7)	0.48	1.48(6)
130.754(7)	140(30)	13.3(2)	-21	10.52(2)
133.04(2)	140(40)	1.82(8)	63	1.76(7)
133.88(2)	60(30)	1.71(8)	0.10	1.64(8)
134.75(5)	60(30)	0.56(4)	0.25	0.55(4)
137.809(8)	250(20)	6.86(3)	0.36	6.4(2)
140.39(2)	60(30)	1.34(7)	0.16	1.30(7)
141.33(5)	80(40)	0.48(4)	0.31	0.47(4)
145.63(1)	140(30)	3.5(1)	0.40	3.4(1)
147.02(1)	130(40)	2.9(1)	0.64	2.8(1)
148.193(9)	140(30)	5.6(2)	0.53	5.2(1)
149.484(8)	70(30)	13.8(5)	-0.97	8.7(3)
150.176(7)	160(20)	15.4(4)	0.48	13.42(3)
152.24(1)	80(30)	3.2(1)	-19	2.9(1)
153.71(6)	150(70)	0.46(4)	0.41	0.47(4)
156.291(9)	100(20)	4.7(1)	0.10	4.4(1)
160.063(9)	90(20)	5.5(1)	-13	5.1(1)
161.616(5)	90(10)	12.4(2)	-0.74	10.3(2)
168.311(7)	70(20)	13.7(4)	-0.98	9.0(2)
170.34(1)	90(30)	5.5(2)	0.20	5.0(1)
171.30(1)	130(30)	5.7(2)	0.39	5.4(2)
173.566(5)	101(12)	21.7(4)	-0.86	16.2(2)
175.44(4)	120(50)	1.10(8)	0.30	1.09(8)
178.01(1)	90(30)	4.1(2)	-35	3.6(1)
180.32(1)	90(120)	6.2(2)	-0.65	5.2(1)

A comparison of the kernels from the present analysis to the ones from evaluations, Ref. [11] and Ref. [17] is reported as a function of resonance energy in Fig. 12 in terms of residuals (i. e. difference of our values to the ones

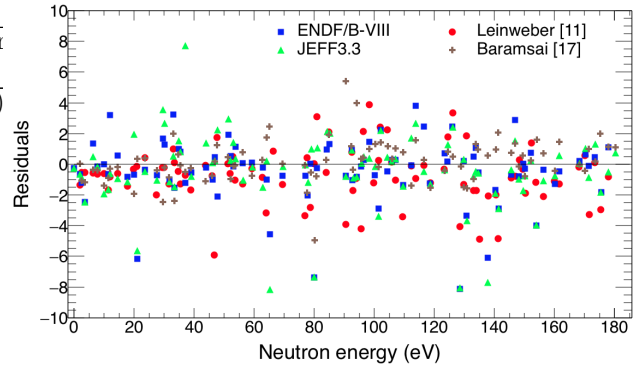


Fig. 12. (Color online) $^{155}\text{Gd}(n,\gamma)$ residuals between the present resonance kernels and values in literature: ENDF/B-VIII.0 and JEFF-3.3 evaluations and TOF experiment reported in Ref. [11] and [17], as a function of neutron resonance energy.

in literature, divided by the uncertainty). On average, a good agreement was found with the ENDF/B-VIII.0 and JEFF-3.3 evaluations, as well as with the resonance parameters by Baramsai *et al.* [17]. Moreover, the statistical distribution of the ratios of our kernels to the others was Gaussian with mean 0.98, 0.98 and 1.02, respectively. On the contrary, the comparison with JENDL-4.0 and the data from Leinweber and collaborators presents an average deviation of about 8%.

The resonances and structures observed in the energy region above RRR are reported in Tab. 7 in Appendix A.1 together with their capture kernels.

4.2 $n+^{157}\text{Gd}$

In the region near thermal energy, the three data libraries ENDF/B-VIII.0, JEFF-3.3 and JENDL-4.0 provide similar values of the capture cross section, between 253.2 and 254.5 kb. In the experiment by Leinweber and collaborators [11], a 12% smaller cross section was deduced. In Figure 13 the present capture yield, obtained with the thin sample, is compared with the expected capture yields calculated from the resonance parameters in evaluations and Ref. [11]. The present data settle in between the two groups of expected values. Our estimation of the thermal cross section, deduced from the resonance parameters of Table 6 is $\sigma_0 = 239.8(8.4)$ kb. As in the case of ^{155}Gd , the Westcott factor sizeably deviates from 1, with a value of 0.89(4), some 5% higher than evaluations.

At higher energies, evaluations show differences and inconsistencies. For instance the spin of the first resonance at 0.032 eV is $J = 2$ in ENDF/B-VIII.0 and JENDL-4.0 while it is $J = 1$ in JEFF-3.3. There are also doubtful resonances at 135.19, 137.9, 202.69, 208.5, 255.2, 300.9 and 306.4 eV, present in the ENDF/B-VIII.0 evaluation (60 resonances in total) which are neither reported in JEFF-3.3 (which contains 56 resonances) nor in JENDL-4.0 (with 54 resonances). Figure 14 shows the energy regions where the largest discrepancies are present. The present

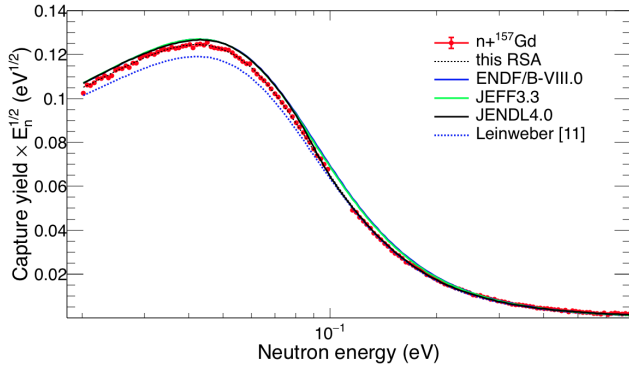


Fig. 13. (Color online) $^{157}\text{Gd}(n,\gamma)$ capture yield (multiplied by $E^{1/2}$) from the thin sample compared with the expected capture yields calculated on the basis of the cross sections in ENDF/B-VIII.0, JEFF-3.3 and JENDL-4.0 libraries and resonance parameters in Ref. [11].

data confirm the resonances in the ENDF/B-VIII.0 evaluation, with the exception of the resonances at 139 eV. Instead of doublet, with resonances at 206.9 and 208.5 eV, we observe a single resonance at 207.725 eV, while the resonance at 220.65 in ENDF/B-VIII.0 is rather a doublet. The results of the resonance shape analysis are summarised in Table 6 where the correlation coefficient between partial widths $\rho(\Gamma_\gamma, \Gamma_n)$, resulting from the SAMMY fit, are also reported. A comparison of the kernels from the present analysis to the ones from evaluations and Ref. [11] is reported as a function of resonance energy in Fig. 15 in terms of residuals. On average a good agreement was found with ENDF/B-VIII.0 and JEFF-3.3 evaluations, since the statistical distribution of the ratios was consistent with a Gaussian with mean 0.98. On the contrary, the comparison with JENDL-4.0 and the data from Leinweber and collaborators does not tend to a Gaussian distribution and the average deviation is 13%.

The resonances and structures observed in the energy region above the upper limit of evaluations are reported in Tab. 8 in Appendix A.1 together with their capture kernel.

4.3 Statistical properties of neutron resonances

Resolved resonance parameters from this analysis, see Tabs. 5 and 6 can be used to determine basic statistical properties of resonances. Since we do not see any significant difference in the number of observed resonances with respect to other experiments reported in literature, the estimation of quantities describing the statistical properties of neutron resonances – s -wave neutron strength function, S_0 , average radiative width, $\bar{\Gamma}_\gamma$, and s -wave average resonance spacing, D_0 – should not differ significantly from nuclear data libraries.

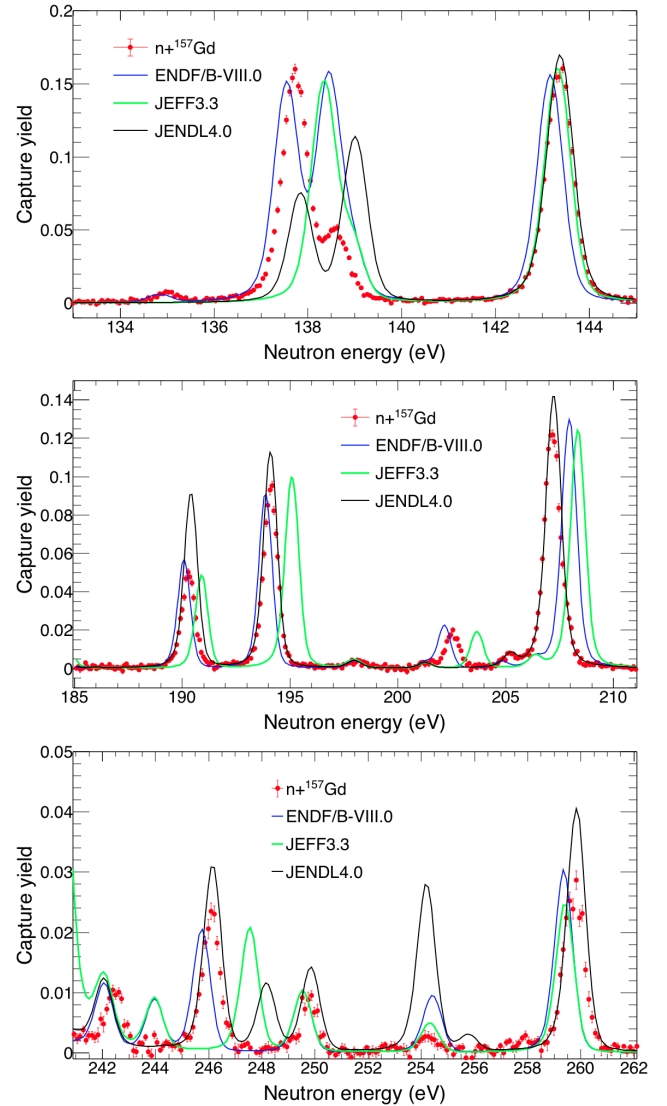


Fig. 14. (Color online) $^{157}\text{Gd}(n,\gamma)$ capture yield obtained with the thick target and comparison with the expected capture yield, calculated on the basis of the cross sections in ENDF/B-VIII.0, JEFF-3.3 and JENDL-4.0 libraries

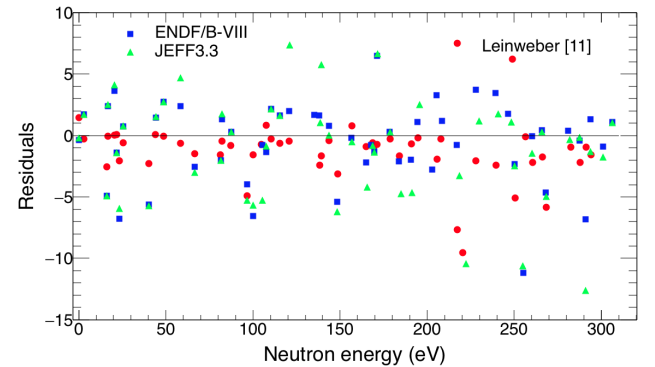


Fig. 15. (Color online) $^{157}\text{Gd}(n,\gamma)$ residuals between resonance kernel of this work and ENDF/B-VIII.0 and JEFF-3.3 evaluations and Ref. [11], as a function of neutron resonance energy.

Table 6. Resonances in $^{157}\text{Gd}(n,\gamma)$. Uncertainties are from the fit. Partial widths are reported for information, capture kernels being the experimental quantity of interest.

Energy (eV)	Γ_γ (meV)	$g\Gamma_n$ (meV)	$\rho(\Gamma_\gamma, \Gamma_n)$	capture kernel (meV)
0.0314	111.80(2)	0.2921(1)	-0.11	0.2908(1)
2.8290(1)	105.9(3)	0.2286(4)	0.16	0.2278(4)
16.219(3)	117(8)	0.114(3)	0.76	0.114(3)
16.7946(2)	102.8(5)	8.73(3)	-0.47	7.685(1)
20.5262(3)	98.8(6)	8.47(2)	-0.49	7.45(2)
21.601(2)	88(6)	0.215(4)	0.66	0.214(4)
23.290(2)	94(5)	0.218(3)	0.58	0.227(3)
25.3653(8)	99(2)	1.176(7)	0.31	1.155(7)
40.091(3)	84(7)	0.354(6)	0.51	0.355(6)
44.1374(8)	101(2)	5.96(3)	-0.02	5.45(2)
48.7076(6)	99(1)	17.3(1)	-0.76	13.52(4)
58.2927(7)	104(2)	20.1(1)	-0.80	15.39(5)
66.536(1)	100(3)	4.45(3)	-0.23	3.98(3)
81.312(2)	121(5)	6.54(5)	0.32	5.72(5)
82.103(3)	91(7)	4.09(5)	0.42	3.81(5)
87.175(2)	78(4)	6.66(6)	-0.41	5.86(5)
96.572(2)	78(4)	6.33(7)	-0.67	5.21(4)
100.160(2)	131(4)	10.7(1)	-0.53	8.78(6)
104.913(2)	156(4)	13.8(9)	-0.29	11.2(7)
107.370(4)	100(11)	3.22(5)	0.36	3.06(5)
110.550(1)	96(6)	31.2(7)	-0.97	20.5(1)
115.373(2)	95(5)	13.9(2)	-0.71	11.28(9)
120.861(2)	100(3)	93(2)	-0.85	37.6(2)
135.35(3)	110(40)	0.64(4)	0.51	0.63(4)
138.088(2)	120(7)	29.4(5)	-0.86	21.1(2)
138.976(6)	120(20)	5.6(1)	0.58	5.3(1)
143.736(2)	109(7)	36.0(9)	-0.96	23.6(2)
148.423(4)	103(9)	6.25(9)	-0.50	5.38(7)
156.592(3)	107(8)	11.8(2)	-0.56	10.1(1)
164.910(3)	82(9)	11.6(3)	-0.93	8.40(9)
168.14(2)	100(40)	1.14(6)	0.53	1.12(5)
169.45(1)	130(40)	1.85(7)	0.64	1.81(7)
171.405(3)	190(10)	21.3(3)	-0.09	16.4(1)
178.727(4)	90(10)	11.0(2)	-0.74	9.2(1)
183.985(4)	90(10)	9.14(2)	-0.84	7.2(1)
190.789(5)	130(10)	8.32(1)	-0.49	7.1(1)
194.614(3)	118(8)	27.06(5)	-0.87	19.8(2)
203.06(1)	90(30)	2.82(8)	-0.04	2.61(7)
205.68(4)	70(40)	0.90(5)	0.16	0.88(5)
207.725(3)	88(4)	125(6)	-0.76	37.7(3)
217.22(1)	80(30)	2.68(8)	-0.30	2.45(7)
220.39(4)	80(40)	0.67(5)	0.25	0.66(5)
221.39(3)	90(40)	1.20(7)	0.33	1.16(7)
228.407(9)	100(20)	5.4(1)	-0.22	5.0(1)
239.572(4)	126(6)	92(5)	-0.82	31.3(4)
243.9(1)	120(50)	0.15(2)	0.12	0.15(2)
246.75(1)	90(20)	6.5(2)	-0.50	5.8(1)
250.42(2)	60(30)	1.76(8)	-0.55	1.62(8)
254.6(1)	100(50)	0.21(4)	0.04	0.21(3)
255.10(8)	110(50)	0.41(5)	0.10	0.406(5)
260.44(1)	114(10)	7.4(2)	-0.06	6.7(2)
265.99(2)	170(30)	4.0(1)	-0.15	3.7(1)
268.44(2)	50(30)	4.9(2)	-0.85	4.2(2)
282.016(6)	90(30)	24.4(7)	-0.90	14.2(2)
287.73(1)	130(30)	8.3(2)	-0.10	7.6(2)
291.070(9)	110(20)	12.3(3)	-0.86	9.5(2)
294.060(6)	89(13)	28(1)	-0.97	15.3(2)
301.353(8)	130(20)	14.9(3)	-0.82	11.5(2)
306.91(4)	110(40)	1.84(1)	0.26	1.8(1)

4.3.1 Neutron strength function

An estimate of the s -wave neutron strength function S_0 can be made from the reduced neutron widths as

$$S_0 = \frac{1}{\Delta E} \sum_{\Delta E} g_J \Gamma_n^0 \quad (4)$$

where ΔE is the interval of neutron energies which the reduced neutron widths Γ_n^0 are summed over. The sum goes over resonances of both spins.

Assuming that the neutron strength function for p -wave resonances is close to the value from systematics in this mass region, $S_1 = 1 - 2 \times 10^{-4}$ [8], no p -wave resonance should be observable in our data as these resonances are too weak. In fact, as already pointed out in Ref. [17], the Porter-Thomas (PT) fluctuations of individual neutron widths almost surely prevent observation of all s -wave resonances in Gd isotopes. Nevertheless, the contribution of these missing resonances to the sum is very small, about 1% in RRR for both nuclei.

The uncertainty in S_0 is given by the uncertainty in individual Γ_n^0 values from SAMMY fitting and by the expected PT fluctuations which the Γ_n^0 values are expected to follow. The PT fluctuation adds an uncertainty $\sqrt{2/N_R} S_0$, where N_R is the number of resonances. Our data yield $S_0 = 2.01(28) \times 10^{-4}$ and $2.17(41) \times 10^{-4}$ for ^{155}Gd and ^{157}Gd , determined from energy regions below 181 and 307 eV, respectively. These values agree with values available in literature: $1.99(28) \times 10^{-4}$ [17] and $2.20(14) \times 10^{-4}$ [8] for ^{155}Gd and $2.20(40) \times 10^{-4}$ [8] for ^{157}Gd . The dominant contribution to the listed uncertainty comes from the Porter-Thomas fluctuations.

Figure 16 shows the dependence of $\sum g_J \Gamma_n^0$ on neutron energy. For resonances where only resonance kernel is given in Tabs. 7 and 8, we assumed $\Gamma_\gamma = 109$ and 105 meV for ^{155}Gd and ^{157}Gd , respectively, when the spin was assigned randomly, assuming that the ratio of the number of $J = 1$ to 2 resonances is 3/5 as expected from standard spin dependence of the level density. Expected uncertainties, corresponding to the average \pm the standard deviation from Porter-Thomas distribution are also indicated in the figure; those for ^{157}Gd are higher due to larger resonance spacing.

4.3.2 Total radiative width

The radiative widths from resonance shape analysis are very precisely determined at low E_n , but their uncertainty significantly increases with neutron energy. The statistical model predicts that due to the many possible decay channels the Γ_γ should not vary much for resonances in a given isotope. This quantity is also expected to depend only weakly on the resonance spin. Simulations of the γ decay of resonances using the DICEBOX code indicated that the fluctuation of Γ_γ are expected to be for resonances with the same spin about 1-2% with a realistic model of nuclear level density and of photon strength functions [32,31]. The simulations also predicted similar

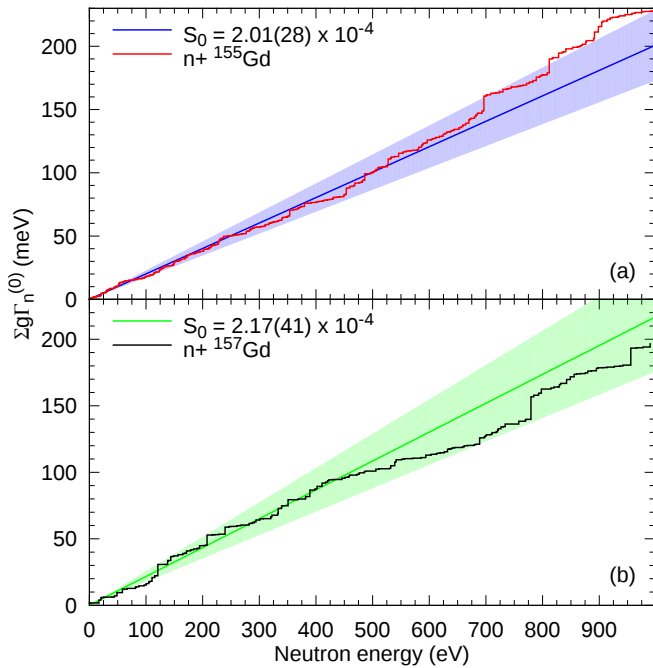


Fig. 16. Cumulative distribution of reduced neutron widths for both Gd isotopes. Solid lines and coloured regions correspond to $S_0 = 2.01(28) \times 10^{-4}$ and $2.17(41) \times 10^{-4}$ deduced from resonances up to 181 and 307 eV in ^{155}Gd and ^{157}Gd , respectively, see also Fig. 2 in Supplemental material.

difference, about 2%, between the Γ_γ expectation values for $J = 1$ and 2 resonances.

Assuming a normal distribution of actual Γ_γ values, we tried to estimate the average value and the width of the distribution of this quantity using the maximum-likelihood (ML) method. Uncertainties of individual values from SAMMY fit were taken into account in determining the parameters of this distribution. Using resonances for $E_n < 50$ eV (i. e. the region where the Doppler broadening is at most 3 times higher than the natural resonance width, see Fig. 9), the ML method yielded the expectation value $\bar{\Gamma}_\gamma = 106.8(14)$ and $101.1(20)$ meV, respectively for ^{155}Gd and ^{157}Gd . These estimations are slightly different from those present in evaluations. For a more detailed discussion of the Γ_γ distribution see the Supplemental material.

4.3.3 Resonance spacing

The cumulative plot of the number of resonances as a function of neutron energy is shown in Fig. 17. The observed deviation from a straight line at higher energies clearly indicates an increasing number of missing levels. We should remind the reader that we are not sure if the reported structures above 181 eV and 307 eV in ^{155}Gd and ^{157}Gd , respectively, correspond to individual resonances. In reality, the PT fluctuations of individual neutron widths almost surely prevent observation of all resonances in Gd isotopes from very low neutron energies (see Supplemental material on this point). The resonance spacing thus

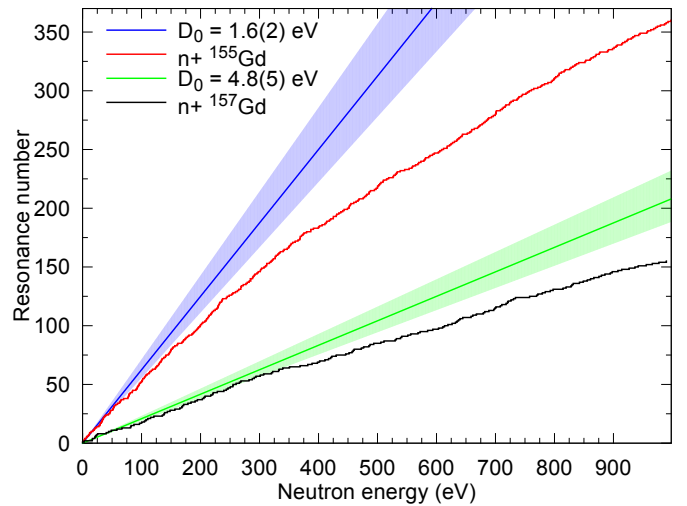


Fig. 17. Cumulative distribution of observed resonances for both Gd isotopes. Blue and green regions correspond to D_0 deduced from our analysis in ^{155}Gd and ^{157}Gd , respectively, see text for details.

cannot be calculated as a simple ratio $\Delta E/N_{obs}$, where N_{obs} is the number of observed resonances, but must be corrected for the unobserved (weak) ones. Many different ways of correction have been applied in the past, see e. g. Refs. [44, 17, 45]. In this work we tried to estimate the spacing using a comparison of the observed number of resonances above some assumed threshold, applied to the resonance kernel, with the predictions of statistical model calculations.

Several thousands of artificial resonance sequences were generated using the above-obtained values of S_0 and $\bar{\Gamma}_\gamma$. The number of observed resonances for several different thresholds and maximum neutron energies (below 400 eV) were nicely consistent with D_0 in the range about 1.4 – 1.8 eV and about 4.3 – 5.3 eV in ^{155}Gd and ^{157}Gd , respectively. These ranges exactly coincide with the average plus/minus one sigma corridor of D_0 obtained with the threshold which corresponds to $10\times$ the equi-probability line from Fig. 1 of the Supplemental material and the maximum neutron energy of 181 and 307 eV in ^{155}Gd and ^{157}Gd , respectively. As a result, we adopt $D_0 = 1.6(2)$ eV and $4.8(5)$ eV for ^{155}Gd and ^{157}Gd , respectively. These values are fully consistent with values available in the literature. The use of higher neutron energies than 400 eV starts to be problematic as reported structures may correspond to close resonance multiplets.

5 Summary

We have reported the results of a new measurement of the capture cross section of the $^{155}\text{Gd}(n,\gamma)$ and $^{157}\text{Gd}(n,\gamma)$ reactions, for $E_n < 1$ keV. The expectation value of thermal cross sections extracted in this work are about 2% higher for ^{155}Gd and 6% smaller for ^{157}Gd in comparison to those reported in nuclear data libraries. These values are consistent within 1.5 standard deviations with the compila-

tion by Mughabghab [8]. For ^{155}Gd , the present result is consistent with the data of Ohno and Leinweber and is compatible with the data of Møller within 1.2 standard deviations. For ^{157}Gd , the present value is consistent with the value reported by Ohno and is compatible with the one of Møller and Leinweber within 1.4 and 1.6 standard deviations, respectively. It is worth to mention that our value could reproduce the integral experiments conducted in 2012 in the Canadian Zed-2 reactor [46]. These tests indeed showed that ENDF/B evaluations overestimate the effect of Gd neutron capture, whereas the value by Leinweber results in an almost symmetric underestimation of neutron capture.

From the R-matrix analysis of the present work, we extracted resonance parameters and cross sections from thermal energy to about 1 keV. The comparisons with ENDF/B-VIII.0 and JEFF-3.3 nuclear data libraries show a fair agreement, in the resolved resonance region, whereas sizeable differences are found with respect to the experiment by Leinweber and collaborators and therefore with the JENDL-4.0 evaluation.

The results of the capture yields obtained in the present measurement, which will be submitted to the EXFOR database, could be used for future evaluations, hopefully in combination with the results of a new transmission experiment.

Acknowledgments

The isotopes used in this research were supplied by the United States Department of Energy Office of Science by the Isotope Program in the Office of Nuclear Physics.

This research was partially funded by the European Atomic Energy Community (Euratom) Seventh Framework Programme FP7/2007-2011 under the Project CHAND (Grant No. 605203).

We acknowledge support from FPA2014-52823-C2-1-P (MINECO)

A Appendix

A.1 : ^{155}Gd and ^{157}Gd resonances not included in evaluations

The present data clearly show structures in the $^{155}\text{Gd}(n,\gamma)$ and $^{157}\text{Gd}(n,\gamma)$ cross sections also above the resolved resonance region reported in the evaluations, as can be seen in Fig. 18. Although these structures might be doublets or even more complicated multiplets, let us call them resonances here.

The properties of these resonances (267 for ^{155}Gd and 96 for ^{157}Gd), namely resonance energy and capture kernel, are reported in Table 7 and 8 up to $E_n = 1$ keV. The resonance analysis was performed with SAMMY, by adopting a constant capture width $\bar{\Gamma}_\gamma = 109$ and 105 meV for $n+^{155}\text{Gd}(n,\gamma)$ and $n+^{157}\text{Gd}(n,\gamma)$ reaction, respectively, and assuming angular orbital momentum $\ell =$

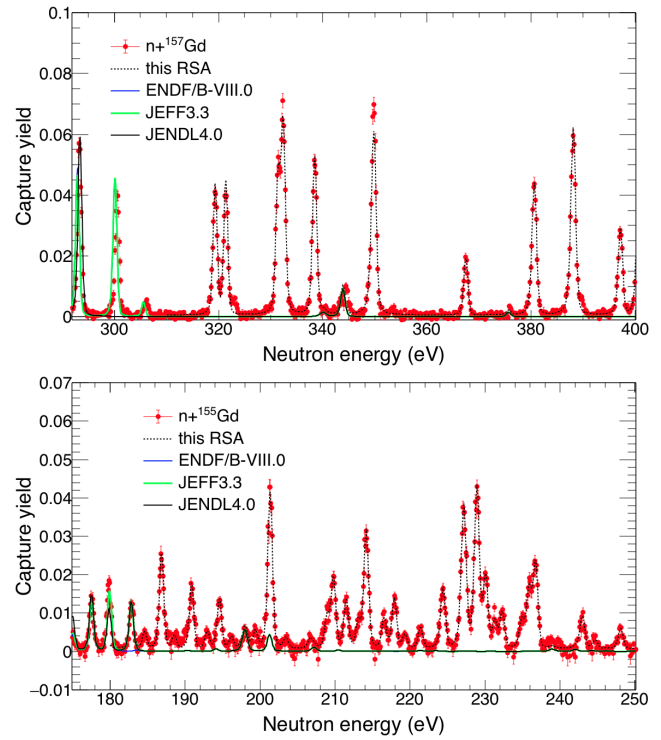


Fig. 18. (Color online) $^{155,157}\text{Gd}(n,\gamma)$ capture yield from the present work and calculated according to ENDF/B-VIII.0, JEFF-3.3 and JENDL-4.0 libraries around the boundary of RRR..

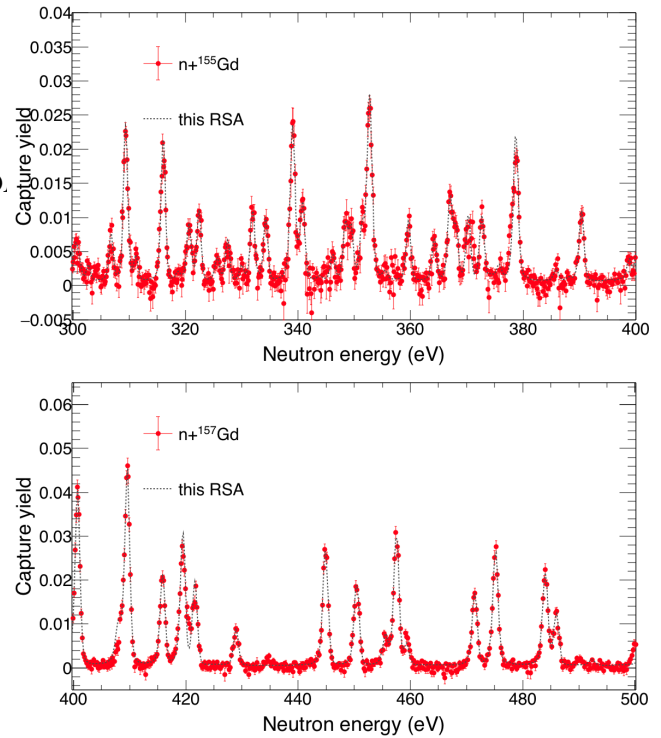


Fig. 19. (Color online) $^{155,157}\text{Gd}(n,\gamma)$ capture yield from the present experiment and the results of the resonance shape analysis.

Table 7: Some properties of the 272 $^{155}\text{Gd}(n,\gamma)$ resonances not included in the evaluations. Uncertainties are from the fit.

Energy (eV)	capture kernel (meV)	Energy (eV)	capture kernel (meV)	Energy (eV)	capture kernel (meV)	Energy (eV)	capture kernel (meV)
185.08(4)	1.33(9)	328.37(4)	4.3(3)	526.20(4)	20.7(1)	738.4(2)	6.0(5)
187.36(1)	8.22(2)	330.86(12)	1.5(1)	527.37(3)	30.2(8)	739.8(3)	1.5(1)
189.05(5)	1.08(8)	332.83(3)	7.5(4)	530.35(9)	4.9(4)	744.05(6)	21(1)
191.37(1)	5.6(2)	335.14(3)	7.0(4)	532.14(5)	13.4(7)	745.9(2)	5.2(4)
193.45(3)	1.45(9)	339.94(2)	18.7(6)	533.44(6)	10.1(6)	751.7(2)	3.9(3)
195.10(1)	4.3(1)	341.75(4)	8.3(4)	538.41(6)	7.3(5)	754.4(3)	2.8(3)
196.68(5)	1.01(7)	347.08(9)	2.9(2)	545.97(3)	32(1)	757.4(1)	9.6(7)
199.1(2)	0.12(1)	349.34(6)	6.3(4)	553.68(4)	16.3(7)	760.9(2)	5.4(4)
199.89(4)	1.49(9)	350.32(6)	6.0(4)	558.5(3)	7.5(6)	764.92(8)	12.2(8)
201.87(1)	14.2(3)	352.30(6)	5.6(4)	559.6(1)	4.9(4)	771.73(7)	19.3(9)
203.97(5)	0.98(8)	353.65(2)	27.7(6)	564.4(2)	2.2(2)	776.49(6)	20(1)
207.20(5)	0.83(7)	356.40(0)	1.0(1)	568.28(6)	9.3(6)	778.9(3)	2.6(2)
209.47(3)	3.0(2)	360.58(3)	7.5(4)	569.9(3)	0.72(7)	783.16(5)	23(1)
210.33(1)	7.2(2)	365.16(5)	5.2(3)	573.7(1)	2.7(2)	788.80(5)	26.9(8)
212.04(2)	4.8(2)	367.99(3)	10.2(5)	578.8(1)	4.3(3)	794.63(9)	12.9(9)
213.64(3)	2.6(2)	368.9(3)	0.40(4)	580.48(7)	12.4(8)	796.5(1)	12.1(8)
214.71(1)	12.5(3)	369.03(6)	6.5(4)	581.40(5)	19.4(9)	798.8(1)	11.2(8)
217.10(2)	2.9(1)	371.23(4)	8.5(4)	586.61(4)	21.2(8)	800.2(3)	2.9(3)
218.48(2)	5.2(2)	373.66(3)	8.7(4)	588.92(4)	17.1(8)	802.1(4)	1.7(2)
219.88(4)	1.4(1)	375.3(2)	0.67(6)	593.29(6)	9.6(5)	805.4(4)	0.47(5)
221.99(3)	2.1(1)	379.68(2)	22.2(6)	596.38(4)	23.0(8)	807.8(3)	5.7(5)
224.99(1)	6.7(2)	386.9(2)	0.87(8)	603.40(6)	9.9(7)	808.20(9)	24(1)
227.77(1)	17.3(3)	386.9(2)	0.68(7)	605.53(6)	10.8(7)	811.81(7)	36.7(4)
229.46(2)	12.0(6)	391.40(3)	10.2(5)	608.7(3)	7.0(8)	816.3(2)	9.5(7)
229.63(4)	7.0(5)	399.89(8)	3.0(2)	612.0(3)	13(1)	818.0(1)	13.4(8)
230.68(2)	8.2(3)	401.56(3)	8.2(4)	616.85(7)	9.5(7)	825.9(4)	0.54(5)
231.90(3)	2.9(2)	405.97(5)	5.0(3)	618.8(2)	1.5(1)	828.28(6)	29.5(8)
232.91(2)	4.2(2)	410.67(6)	5.2(3)	622.1(3)	1.1(1)	831.4(4)	1.2(1)
235.52(3)	3.1(2)	412.96(7)	3.4(3)	624.50(4)	20.5(8)	834.44(9)	14.2(8)
236.48(2)	6.9(3)	414.22(4)	8.4(5)	627.22(6)	12.8(7)	837.3(2)	8.4(7)
237.35(1)	10.4(3)	418.50(9)	2.7(2)	630.55(4)	16.5(6)	841.01(7)	25.6(9)
243.63(2)	3.9(2)	420.53(8)	4.7(3)	634.2(1)	4.8(4)	851.7(2)	7.3(6)
245.35(7)	0.98(8)	425.1(1)	4.4(3)	635.6(4)	0.92(9)	853.07(9)	16.3(9)
248.74(3)	2.5(1)	425.2(3)	1.7(2)	638.10(6)	14.0(8)	860.60(3)	4.3(4)
252.8(1)	0.77(7)	430.07(2)	19.1(7)	640.69(9)	8.0(5)	862.3(2)	7.7(6)
254.79(2)	5.9(2)	430.8(1)	3.0(3)	643.3(1)	8.1(6)	865.92(8)	16.8(9)
259.15(3)	2.4(2)	434.4(2)	1.2(1)	644.13(8)	9.6(6)	869.3(1)	15.3(9)
262.51(3)	2.9(2)	437.61(7)	4.4(3)	652.36(4)	21.9(9)	870.8(2)	9.3(7)
264.84(3)	3.5(2)	440.98(7)	3.8(3)	656.26(6)	14.8(7)	875.96(8)	25(1)
268.4(2)	1.0(1)	443.4(1)	2.4(2)	659.17(7)	17(1)	876.97(9)	21(1)
268.38(9)	2.9(2)	449.21(2)	21.4(7)	659.6(2)	7.1(6)	890.1(1)	23(1)
269.37(4)	2.6(2)	452.03(8)	4.8(3)	664.19(4)	23.7(9)	891.45(6)	48(1)
272.34(4)	2.7(2)	452.1(4)	4.8(4)	669.76(5)	25.9(8)	898.44(7)	31.5(7)
276.96(1)	17.4(4)	453.5(5)	29.1(9)	671.66(6)	17(1)	901.2(1)	1.9(2)
279.27(6)	1.8(1)	454.7(3)	6.4(5)	674.0(1)	8.1(6)	904.29(6)	29.8(8)
282.52(1)	13.5(3)	459.75(3)	19.2(7)	677.2(4)	0.86(8)	906.5(4)	15(1)
285.17(3)	6.0(3)	463.8(2)	1.8(2)	679.86(5)	19.6(8)	913.91(9)	22(1)
284.34(3)	6.5(3)	467.19(4)	12.5(6)	682.45(4)	24(1)	915.43(4)	8.6(7)
288.09(2)	7.3(3)	468.62(3)	24.2(8)	684.84(5)	17.0(7)	919.4(1)	23(1)
288.99(4)	4.8(3)	475.70(8)	5.2(4)	686.8(3)	1.4(1)	923.0(2)	11.6(8)
290.85(7)	1.2(1)	477.97(6)	6.5(5)	688.4(4)	0.94(9)	924.7(5)	0.60(6)
292.36(2)	5.9(3)	480.58(9)	3.8(3)	693.22(4)	29(1)	930.4(5)	0.46(5)
295.71(8)	1.3(1)	482.26(2)	22.6(8)	696.36(6)	36.7(4)	932.9(1)	12.6(8)

Continued on next page

0. Examples of the quality of the resonance shape analysis are shown in Fig. 19.

Table 7 (Continued)

Energy (eV)	capture kernel (meV)	Energy (eV)	capture kernel (meV)	Energy (eV)
297.7(1)	0.99(9)	485.6(2)	1.7(2)	699.74(5)
301.25(5)	3.0(2)	487.97(3)	30.1(6)	700.7(3)
301.93(8)	1.8(2)	485.9(3)	1.3(1)	701.0(2)
303.57(7)	1.5(2)	494.8(1)	2.9(2)	701.4(4)
307.60(4)	4.5(3)	497.77(5)	10.0(5)	708.28(5)
310.20(1)	16.0(4)	499.99(9)	6.9(6)	711.3(4)
311.98(8)	2.2(2)	500.17(8)	7.7(7)	713.4(4)
312.3(3)	0.36(4)	502.18(7)	6.0(4)	716.6(2)
316.88(1)	15.0(4)	503.77(6)	6.6(4)	717.5(2)
319.5(2)	0.72(7)	505.86(3)	17.5(6)	723.5(1)
321.50(3)	5.9(3)	509.43(4)	16.0(9)	724.1(2)
323.27(2)	7.4(3)	510.02(6)	11.3(7)	726.6(4)
326.4(2)	1.4(1)	515.3(1)	4.1(3)	730.15(4)
326.6(2)	1.2(1)	518.82(7)	5.5(4)	736.6(1)

References

1. F. Käppeler, R. Gallino, S. Bisterzo, Wako Aoki, Rev. Mod. Phys. **83**, 157 (2011)
2. [2] A. Deagostino, *et al.*, Future Med Chem. **8**, 899 (2016)
3. J. F. Beacom and M. R. Vagins, Phys. Rev. Lett. **93**, 171101 (2004)
4. F. Rocchi, A. Guglielmelli, D. M. Castelluccio and C. Massimi, Eur. Phys. J. Nuclear Sci. Technol. **3**, 21 (2017)
5. D. A. Brown, *et al.*, Nucl. Data Sheets **148**, 1 (2018)
6. OECD/NEA Data Bank, "The JEF-3.3 Nuclear Data Library" available online at <http://www.oecd-neo.org/dbdata/JEFF33/>
7. K. Shibata, *et al.*, J. Nucl. Sci. Technol. **48**, 1 (2011)
8. S. F. Mughabghab, Atlas of Neutron Resonances (Elsevier, Amsterdam, 2006)
9. H. Bjerrum Møller, F. J. Shore, and V. L. Sailor, Nucl. Sci. Eng. **8**, 183 (1960)
10. Y. Ohno, *et al.*, Japanese report to EANDC, Number 10, p. 1 (1968)
11. G. Leinweber, *et al.*, Nucl. Sci. Eng. **154**, 261 (2006)
12. N. J. Pattenden, Second Internat. At. En. Conf., Geneva 1958, Vol.16, p.44
13. R. B. Tattersall, *et al.*, Journal of Nuclear Energy A **12**, 32 (1960)
14. H.D.Choi, *et al.*, Nucl. Science & Eng. **177**, 219 (2014)
15. G. Noguere, P. Archier, A. Gruel, P. Leconte and D. Bernard, Nucl. Instrum. & Methods A **629**, 288 (2011)
16. Y.-R. Kang, M. W. Lee, G. N. Kim, T.-I. Ro, Y. Danon, D. Williams, G. Leinweber, R. C. Block, D. P. Barry and M. J. Rapp, Nucl. Sci. Eng. **180**, 86 (2015)
17. B. Baramsai, *et al.*, Phys. Rev. C **85**, 024622 (2012)
18. C. Guerrero, *et al.*, Eur. Phys. J. A **49**, 27 (2013)
19. S. Lo Meo, *et al.*, Eur. Phys. J. A **51**, 160 (2015)
20. P. Schillebeeckx, *et al.*, Nucl. Data Sheets **113**, 3054 (2012)
21. P. F. Mastinu, *et al.*, New C₆D₆ detectors: reduced neutron sensitivity and improved safety n_TOF-PUB-2013-002; CERN-n_TOF-PUB-2013-002 (2013)
22. A. Borella, G. Aerts, F. Gunsing, M. Moxon, P. Schillebeeckx, and R. Wynants, Nucl. Instrum. & Methods A **577**, 626 (2007)

Table 8. Some properties of the 96 $^{157}\text{Gd}(n,\gamma)$ resonances not included in the evaluations. Uncertainties are from the fit.

Energy (eV)	capture kernel (meV)	Energy (eV)	capture kernel (meV)	Energy (eV)	capture kernel (meV)	Energy (eV)	capture kernel (meV)
320.19(1)	17.6(3)	487.28(3)	6.6(3)	658.71(4)	11.5(5)	814.73(4)	17.6(8)
322.23(1)	14.034(2)	493.59(3)	0.87(08)	661.62(4)	14.9(6)	819.84(5)	14.4(7)
332.30(2)	17.55(6)	505.67(1)	17.9(4)	667.67(6)	5.6(4)	828.1(2)	3.8(3)
333.29(1)	25.2(5)	511.02(4)	6.7(3)	679.42(5)	11.4(6)	829.62(4)	27.9(9)
339.37(1)	23.9(4)	529.90(3)	6.4(3)	681.69(6)	8.8(5)	831.84(5)	19.0(8)
350.74(1)	27.0(4)	531.87(2)	26.8(5)	688.84(2)	42.8(9)	842.40(3)	37.0(9)
368.48(2)	9.3(3)	538.99(2)	24.6(5)	697.15(4)	14.1(5)	849.02(4)	31(1)
381.67(1)	18.7(3)	541.33(2)	25.1(6)	698.73(6)	12.3(6)	855.72(3)	30.8(9)
389.16(1)	39.5(5)	551.33(3)	8.6(3)	700.64(4)	17.8(7)	861.1(1)	8.2(5)
398.24(1)	12.1(3)	556.16(4)	7.8(3)	708.24(7)	5.5(3)	866.7(1)	5.1(4)
401.78(1)	24.1(4)	568.49(8)	3.0(2)	710.64(2)	19.5(6)	875.46(8)	12.8(7)
410.67(1)	22.2(4)	572.13(5)	5.1(3)	718.04(5)	11.8(6)	879.67(3)	24.7(8)
416.97(2)	12.2(4)	584.93(4)	8.7(4)	720.49(5)	21.5(9)	885.6(1)	6.3(5)
420.57(1)	14.1(3)	593.79(2)	21.3(5)	721.59(4)	20.8(9)	894.79(4)	30(1)
422.78(2)	11.4(3)	603.41(3)	12.1(5)	726.31(3)	23.9(7)	897.79(7)	11.0(6)
430.07(3)	5.0(2)	610.44(9)	2.4(2)	730.52(8)	5.2(4)	907.48(4)	5.5(5)
446.05(1)	13.7(3)	613.54(3)	12.4(4)	733.88(3)	29.0(8)	914.08(9)	7.6(4)
451.64(2)	11.8(4)	619.32(5)	6.5(4)	757.80(2)	31.0(8)	926.70(7)	14.2(7)
456.75(4)	4.4(2)	626.50(3)	14.9(5)	769.81(3)	23.5(7)	936.46(1)	7.5(5)
458.72(1)	16.0(3)	632.22(2)	21.8(5)	771.0(2)	3.2(3)	941.99(5)	12.9(6)
460.78(1)	2.6(3)	635.00(8)	3.8(3)	779.48(3)	56.2(5)	955.65(3)	55.2(7)
472.70(2)	11.6(4)	637.29(1)	2.6(2)	784.34(3)	22.6(8)	965.91(1)	6.9(5)
476.40(1)	14.5(3)	639.72(3)	11.5(4)	792.90(3)	25.8(8)	977.24(8)	13.9(8)
485.29(2)	15.8(4)	644.47(4)	8.8(4)	797.78(3)	37.9(9)	989.79(4)	35(1)

23. M. Barbagallo, *et al.*, Eur. Phys. J. A **49**, 156 (2013)
24. A. D. Carlson, *et al.*, Nucl. Data Sheets **110**, 3215 (2009)
25. S. Marrone, *et al.*, Nucl. Instrum. & Methods A **517**, 389 (2004)
26. J. Allison, *et al.*, Nucl. Instrum. & Methods A **835**, 186 (2016)
27. F. Bečvář, Nucl. Instrum. Methods A **417**, 434 (1998)
28. C. W. Reich, Nucl. Data Sheets **99**, 753 (2003)
29. R. G. Helmer, Nucl. Data Sheets **101**, 325 (2004)
30. H. Xiaolong and K. Mengxiao, Nucl. Data Sheets **133**, 221 (2016)
31. A. Chyzh, *et al.*, Phys. Rev. C **84**, 14306 (2011)
32. B. Baramsai, *et al.*, Phys. Rev. C **87**, 44609 (2013)
33. M. Krtićka *et al.*, AIP Conference Proceedings **831**, 481 (2006)
34. T. Kibédi *et al.*, Nucl. Instrum. Methods A **589**, 202 (2013)
35. T. T. Böhlen, *et al.*, Nuclear Data Sheets **120**, 211 (2014)
36. A. Ferrari, *et al.*, "FLUKA: a multi-particle transport code" CERN-2005-10 (2005), INFN/TC_05/11, SLAC-R-773
37. I. Sirakov, *et al.*, "Evaluation of neutron induced reaction cross sections on gold", JRC report 78690 EUR 25803
38. R. L. Macklin, J. Halperin, and R. R. Winters, Nucl. Instrum. & Methods **164**, 213 (1979)
39. N. M. Larson, "Updated Users Guide for SAMMY: Multilevel Rmatrix Fits to Neutron Data Using Bayes Equations, SAMMY" Computer Code, Report No. ORNL/TM-9179/R7, Oak Ridge National Laboratory, 2008
40. C. Massimi, *et al.*, Eur. Phys. J. A (2014) 50:124
41. P. Archier *et al.*, "CONRAD evaluation code: Development Status and Perspectives", Proc. Int. Conf. Nuclear Data for Science and Technology, New-York, USA (2013)
42. M.C. Moxon and J.B. Brisland, "GEEL REFIT, A least squares fitting program for resonance analysis of neutron transmission and capture data computer code", In Tec-0630, AEA Technology, October (1991)
43. C. Massimi, *et al.*, Phys. Rev. C **81**, 044616 (2010)
44. G. E. Mitchell, J. F. Shriner, "Missing Level Corrections using Neutron Spacings", IAEA Technical Report INDC(NDS)-0561 (2009)
45. <https://www.oecd-neo.org/tools/abstract/detail/nea-0892/>
46. J. C. Chow, F. P. Adams, D. Roubtsov, R. D. Singh, M. B. Zeller, AECL Nuclear Review, **1**, 21 (2012)